Cell

A line attractor encoding a persistent internal state requires neuropeptide signaling

Graphical abstract

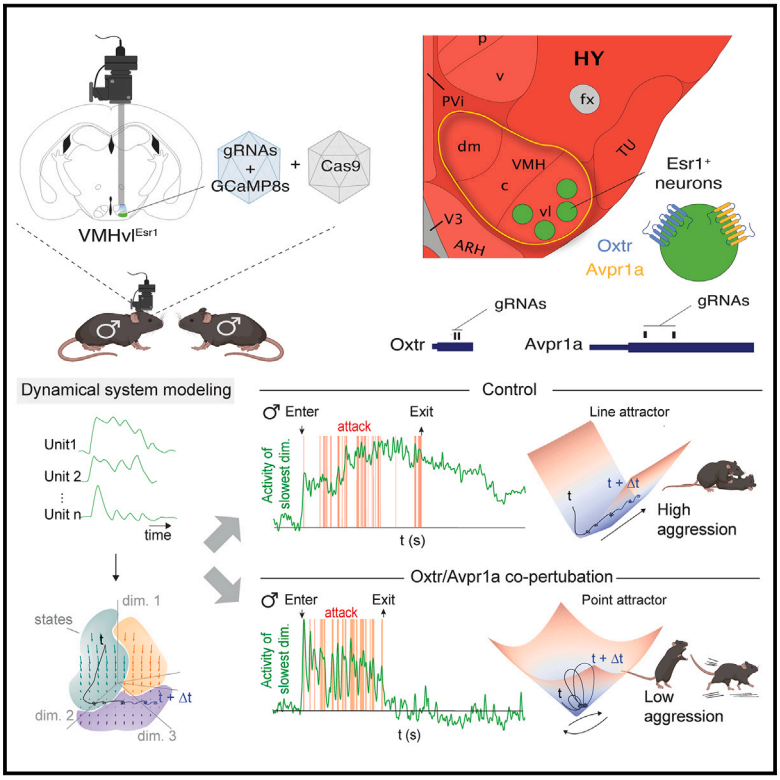

Highlights

- "CRISPRoscopy" integrates calcium imaging and gene editing in the same neuronal cell type
- Co-editing of *Oxtr* and *AVPr1a* genes in VMH^{Esr1} neurons reduces aggression but not mounting
- A line attractor encoding a scalable, persistent aggressive internal state is eliminated
- Line attractor implementation in the hypothalamus requires neuropeptide signaling

Authors

George Mountoufaris, Aditya Nair, Bin Yang, ..., Samuel Kim, Scott W. Linderman, David J. Anderson

Correspondence

wuwei@caltech.edu

In brief

Oxytocin and vasopressin receptors are required in the ventromedial hypothalamus for persistent neural activity and line attractor dynamics that encode an aggressive internal state.

Mountoufaris et al., 2024, Cell *187*, 5998–6015
October 17, 2024
https://doi.org/10.1016/j.cell.2024.08.015

CellPress

CellPress
OPEN ACCESS

Cell

Article

A line attractor encoding a persistent internal state requires neuropeptide signaling

George Mountoufaris,[1,3] Aditya Nair,[1,2,3] Bin Yang,[1,3,7] Dong-Wook Kim,[1,3,8] Amit Vinograd,[1,3] Samuel Kim,[1,3] Scott W. Linderman,[5,6] and David J. Anderson[1,3,4,9,*]

[1]Division of Biology and Biological Engineering, California Institute of Technology, Pasadena, CA, USA
[2]Program in Computation and Neural Systems, California Institute of Technology, Pasadena, CA, USA
[3]Tianqiao and Chrissy Chen Institute for Neuroscience, California Institute of Technology, Pasadena, CA, USA
[4]Howard Hughes Medical Institute, Pasadena, CA 91001, USA
[5]Department of Statistics, Stanford University, Stanford, CA 94305, USA
[6]Wu Tsai Neurosciences Institute, Stanford University, Stanford, CA 94305, USA
[7]Present address: Johns Hopkins University School of Medicine, Baltimore, MD, USA
[8]Present address: Allen Institute for Brain Science, Seattle, WA, USA
[9]Lead contact
*Correspondence: wuwei@caltech.edu
https://doi.org/10.1016/j.cell.2024.08.015

SUMMARY

Internal states drive survival behaviors, but their neural implementation is poorly understood. Recently, we identified a line attractor in the ventromedial hypothalamus (VMH) that represents a state of aggressiveness. Line attractors can be implemented by recurrent connectivity or neuromodulatory signaling, but evidence for the latter is scant. Here, we demonstrate that neuropeptidergic signaling is necessary for line attractor dynamics in this system by using cell-type-specific CRISPR-Cas9-based gene editing combined with single-cell calcium imaging. Co-disruption of receptors for oxytocin and vasopressin in adult VMH Esr1^{+} neurons that control aggression diminished attack, reduced persistent neural activity, and eliminated line attractor dynamics while only slightly reducing overall neural activity and sex- or behavior-specific tuning. These data identify a requisite role for neuropeptidergic signaling in implementing a behaviorally relevant line attractor in mammals. Our approach should facilitate mechanistic studies in neuroscience that bridge different levels of biological function and abstraction.

INTRODUCTION

Innate survival behaviors such as aggression, mating, feeding, and defense are driven by internal motivational or affective states,[1–3] which are experienced in humans as subjective feelings.[4,5] How and where such internal states are encoded in the brain, and how they are causally related to overt behavior, is emerging as a major topic in circuit and systems neuroscience.[6,7]

The study of internal states has been pursued via two approaches that have, until recently, remained relatively separate. One, a "bottom-up" approach, employs genetically or pharmacologically based manipulations of genes and neural circuits[6,8,9] aimed at providing causal explanations for behavioral and psychological internal states.[10–12] The other, a "top-down" approach, identifies internal states computationally in high-dimensional neural population activity.[13,14] The latter has revealed attractors as a mechanism for encoding low-dimensional variables underlying cognitive functions.[15–19] More recently, such models have been applied in behavioral neuroscience as well.[20–22] To test the causal role of such attractors, it is important to understand their neural implementation at the level of cell types and genes. This in turn requires integration of these two approaches,[23] which has been accomplished in very few systems.[24,25]

Persistent neural activity (on a timescale of seconds to minutes) is a characteristic feature of neural integrators and attractor dynamics.[18,26,27] Two alternative (but not mutually exclusive) implementation mechanisms are typically invoked to explain such persistence: recurrent fast synaptic connectivity or slow neuromodulation.[28] While there is evidence of recurrent connectivity underlying a ring attractor that encodes head direction in *Drosophila*,[24,25,29] to our knowledge, there is no evidence of any neuromodulator that controls attractor dynamics in any system.

Neuropeptides comprise a class of evolutionarily conserved neuromodulators[30,31] that control behavior-specific internal motive states associated with mating,[32,33] aggression,[34–36] social attachment,[37] and other behaviors. Neuropeptides are well known to modulate synaptic strength and neural circuit properties such as patterns of oscillation,[38–40] but their role in implementing neural integrator and attractor dynamics has not been extensively studied in vertebrates. Experiments in

C. elegans have identified neuropeptides that control persistent states of locomotor activity,[41,42] but whether they influence the dynamical manifolds identified in that system[43] is not yet clear.

A powerful approach to this question is to combine cell type-specific genetic perturbations of neuromodulatory signaling with simultaneous large-scale recording of neural activity in the same brain region and genetically defined cell type. While these experimental modalities have been successfully integrated in *C. elegans*,[42,44] *D. melanogaster*[45,46] and larval zebrafish,[47] they have been difficult to combine in mammalian systems for technical reasons (Figure S1A).

Here we describe a viral-based strategy that integrates cell-type-specific, regionally restricted CRISPR-Cas9-based multiplex gene editing[48,49] with single-unit-resolution calcium imaging of neural dynamics in freely behaving adult animals,[50] which we call "CRISPRoscopy." This method, when combined with dynamical systems modeling,[51,52] allows investigation of the effects of local inactivation of different neuromodulatory receptors on neural population coding, dynamics, and behavior in the same brain region and cell type during naturalistic behaviors.

As a proof-of-concept application of this approach, we have examined the role of oxytocin (OXT) and arginine vasopressin (AVP) signaling in a population of neurons in the ventromedial hypothalamus (VMH) that controls aggression.[53,54] We chose these peptides for several reasons. First, they have been widely implicated in the control of social behaviors[37,55] (although the role of OXT in aggression has been controversial[56–58]). Second, VMH neurons are known to express receptors for OXT and AVP,[59,60] and infusion of the latter into VMH can enhance aggression in hamsters.[61] Third, aggression is an instinctive and phylogenetically widespread social behavior that expresses an internal affective state.[62,63] Finally, dynamical systems modeling[51,52] of population activity from estrogen receptor-1 (Esr1)-expressing neurons in the ventrolateral subdivision of the VMH (VMHvl^{Esr1})[64] has revealed an approximate line attractor (or leaky integrator). This attractor is intrinsic to VMHvl[65] and represents a scalable, persistent aggressive internal state.[21]

Here, we show that genetic perturbation of OXT and AVP receptors in VMHvl^{Esr1} neurons disrupts aggressive behavior, persistent activity, and line attractor dynamics while only modestly affecting overall neuronal activity and population coding of behavior or intruder sex.[66] These data provide evidence of a requirement for neuropeptides in line attractor dynamics and strengthen the link between such dynamics and an internal affective state.

RESULTS

Most Esr1$^+$ neurons co-express OXT and vasopressin receptors and respond to these peptides *ex vivo*

To determine whether Oxtr and Avpr1α receptors are co-expressed in individual VMH neurons, we examined a single-cell RNA-seq (scRNA-seq)-based atlas of VMHvl transcriptomic cell types[67] anatomically validated by smFISH.[68] We observed co-expression of *Oxtr* and *Avpr1α* mRNA transcripts (but not of *Avpr1β* or *Avp2r* transcripts) within individual neurons belonging to several Esr1$^+$ transcriptomic clusters (Figures 1B, S1B, and S1E). All Esr1$^+$ VMHvl clusters contained cells expressing *Oxtr*, with most clusters (5/8) containing cells that co-expressed *Avpr1a* transcripts (Figures 1C, 1D, and S1C). Overall, ~78% of Esr1$^+$ cells in VMHvl expressed *Oxtr* mRNA, and ~61% of these cells also expressed Avpr1a mRNAs (Figure 1E). However, none of the VMHvl clusters expressed *Oxt* or *Avp* transcripts, indicating that the source(s) of the peptides must be extrinsic to the nucleus[69] (Figure S1D).

To explore the effect of OXT and AVP on the physiological activity of VMHvl neurons, we used 2-photon imaging of acute VMH slice preparations (Figure 1Fi). This system enabled us to record Ca^{2+} traces in brain slices from ESR1-2A-CRE animals[64] expressing a CRE-dependent Ca^{2+} indicator (GCaMP7f).[72] Perfusing a mixture of 400 nM (each) OXT plus AVP or individually administering these peptides elicited strong ($\Delta F/F$ ~500%–600%) responses in VMHvl^{Esr1} cells (Figures 1Fii, S1F, and S1G). These findings demonstrated the presence of functional AVP and OXT receptors in VMH neurons, consistent with prior electrophysiological studies.[69,73,74] Furthermore, it established a high-yield system for evaluating cellular responses to OXT and AVP following CRISPR-Cas9-based mutations of their receptors.

Oxtr/Avpr1a-mediated neuropeptidergic signaling in VMH is required for male territorial aggression

The likelihood of functional redundancy or developmental compensation between OXTR and AVPR1a in mediating responses to OXT and/or AVP[73,75] prompted us to design a multiplex viral CRISPR-Cas9 approach to concurrently target both receptors in the same cells. To do this, we modified previously described vectors[76] to express two different gRNAs targeting *Oxtr* and *Avpr1a* from four distinct RNA polymerase III promoters in either a lentiviral (LV) or an adeno-associated virus (AAV) vector (Figure 2A; see STAR Methods). We used two different gRNAs for each receptor gene since this approach has been reported to significantly increase *in vivo* gene editing efficiency in the mammalian nervous system.[77] Each gRNA was designed to target either the *Oxtr* or the *Avpr1a* coding region, and this specificity was confirmed using the T7 endonuclease assay[78] (Figure S2A). Editing efficiency as measured by sequence trace decomposition[79] varied from 32%–81%, depending on the gRNA.

While OXT, AVP, and their receptors have been studied extensively in rodent aggression using pharmacologic reagents and zygotic gene knockouts,[32,56,80–83] there are no reports of a specific requirement in offensive aggression for either *Oxtr* or *Avpr1a* in murine VMHvl. Because local infusion of pharmacological blockers cannot currently be combined with microendoscope imaging,[50,84] we initially sought to use CRISPR-Cas9-mediated gene editing to evaluate whether these receptors are functionally relevant to this behavior in VMH *in vivo*. Generating viruses with the high titers necessary for *in vivo* applications (see STAR Methods) precluded the inclusion of a Cas9 cDNA in the same vector that encoded two different gRNAs, each against *Oxtr* and *Avpr1a*. Therefore, Cas9 was delivered by co-injection of a separate AAV (Figure 2Aii). To target VMHvl neurons broadly for this initial experiment, we employed a constitutive version of the system. We used an LV-based vector to express the 4 different gRNAs because we found that their anatomical spread is more restricted than that of AAVs.

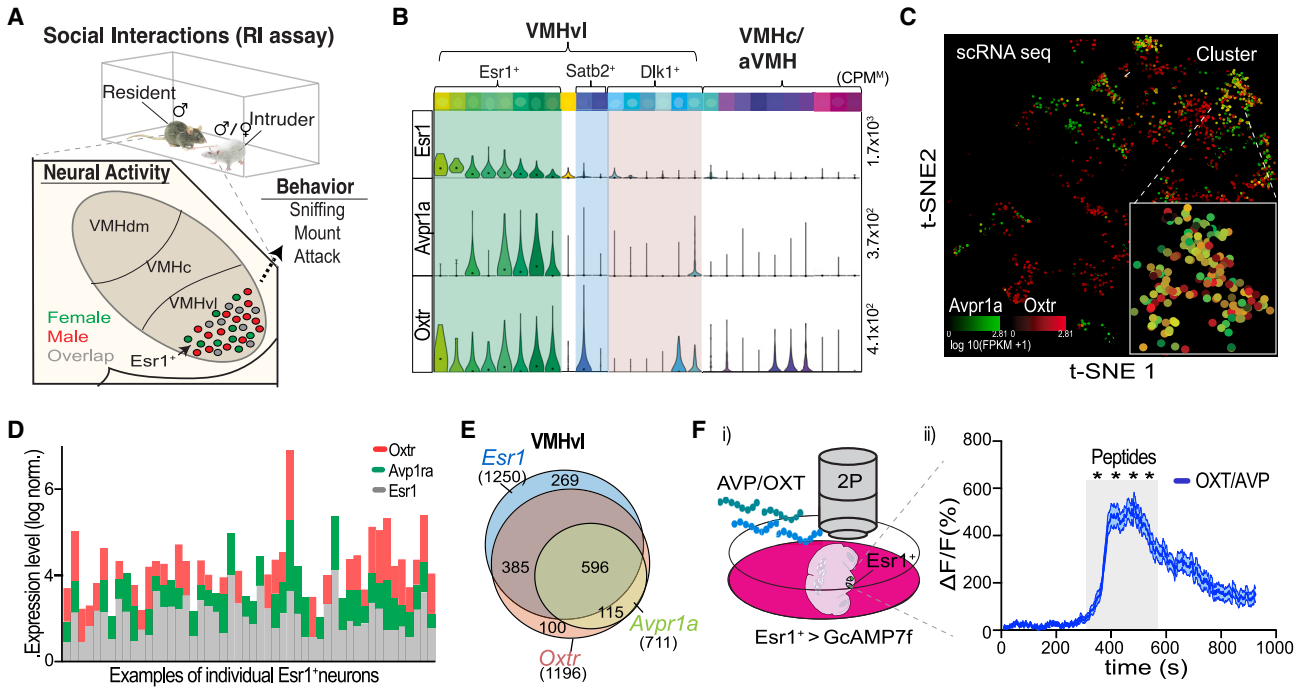

Figure 1. VMHvl^{Esr1} neurons co-express oxytocin and vasopressin receptors and respond to these peptides *ex vivo*

(A) Schematic illustrating resident-intruder (RI) behavioral assay and anatomy of VMH, with dorsomedial (dm), central (c), and ventrolateral (vl) subdivisions indicated. Esr1$^+$ neurons in VMHvl respond specifically to intruder males (red), females (green), or to both (gray).[66] Male- vs. female-tuned neurons control male- vs. female-directed aggression and mating behaviors, respectively.[64,70,71]

(B) Violin plots illustrating expression of *Esr1*, *Avpr1a*, and *Oxtr* mRNAs in VMH single-cell transcriptomic clusters[68] (top, colored boxes) and super-types (shaded regions). CPM^M, maximum counts per million reads.

(C) t-SNE plots illustrating the expression of *Avpr1a* and *Oxtr* mRNAs in single VMH cells (dots). Inset, cluster of Esr1$^+$ cells (see also Figure S1C).

(D) Levels of *Esr1*, *Avpr1a*, and *Oxtr* mRNA expression in ~50 VMH cells.

(E) Venn diagram of *Esr1*, *Avpr1a*, and *Oxtr* mRNA-expressing VMHvl neurons. Circle sizes represent relative number of neurons.

(F) Illustration of two-photon *ex vivo* calcium imaging preparation showing (i) perfusion of brain slices with peptides (400 nM each AVP plus OXT) and (ii) average calcium responses in Esr1$^+$ cells (n = 124 cells, 4 = mice). Gray shaded box depicts peptide perfusion period.

Statistics: values plotted as mean ± SEM. ****$p < 0.0001$, Mann-Whitney test.

See also Figure S1.

Immunohistochemistry of brain sections from animals co-injected with the gRNA-dsRed LV and the Cas9 AAV indicated that ~80% of Cas9$^+$ cells were co-infected with the gRNA virus (Figures 2C and 2D). Assessing the efficiency of co-disrupting both receptors *in vivo* at the protein level was not feasible since staining with available antibodies to OXTR or AVPR1a yielded no signal even in control sections. mRNA levels are not necessarily reduced by CRISPR-Cas9 indels.[85] Therefore, we used calcium imaging in acute VMH brain slices perfused with OXT + AVP to confirm that physiological responses to the peptides were strongly reduced by co-editing of their receptors (see below; Figures 2E and S3B).

We investigated the effect of *Oxtr*/*Avpr1a* co-editing on social behaviors in mice injected in VMH bilaterally with the OAR-gRNA LV and a Cas9 AAV (experimental group) using a standard resident intruder (RI) assay (Figure 1A). We used single-housed, sexually experienced wild-type C57BL/6N resident males pre-selected for adequate aggressiveness (Figure 2F; see STAR Methods). Control animals were co-injected bilaterally with the scrambled gRNA (Scr gRNA) and Cas9 viruses (control group). Experimental mice displayed a notable reduction in aggression toward male intruders, as evidenced by significant decreases in the number and time-varying probability of attack bouts, the total time spent attacking, and the average duration of each attack bout. In addition, the latency to the 1st attack bout was significantly increased (Figures 2Gi, 2Gii, S2B, S2Ci, and S2Cii). These behavioral effects were not due to defects in locomotor activity since average velocity during attack episodes was similar between experimental and control mice (Figure S2Ciii). By contrast, the time spent in close investigation (sniffing) of male intruders did not differ significantly between experimental and control male residents (Figure 2Giii). Experimental males also did not differ significantly from controls in their sniffing or mounting behavior toward female intruders (Figures 2H and S2D).

These data suggest that *Oxtr* and/or *Avpr1a* expressed in VMHvl neurons play a requisite and selective role in aggressive behavior. Furthermore, they motivated us to analyze next how disrupting these receptors specifically in Esr1 neurons affects behavior, neural activity, population coding, and network dynamics *in vivo*.

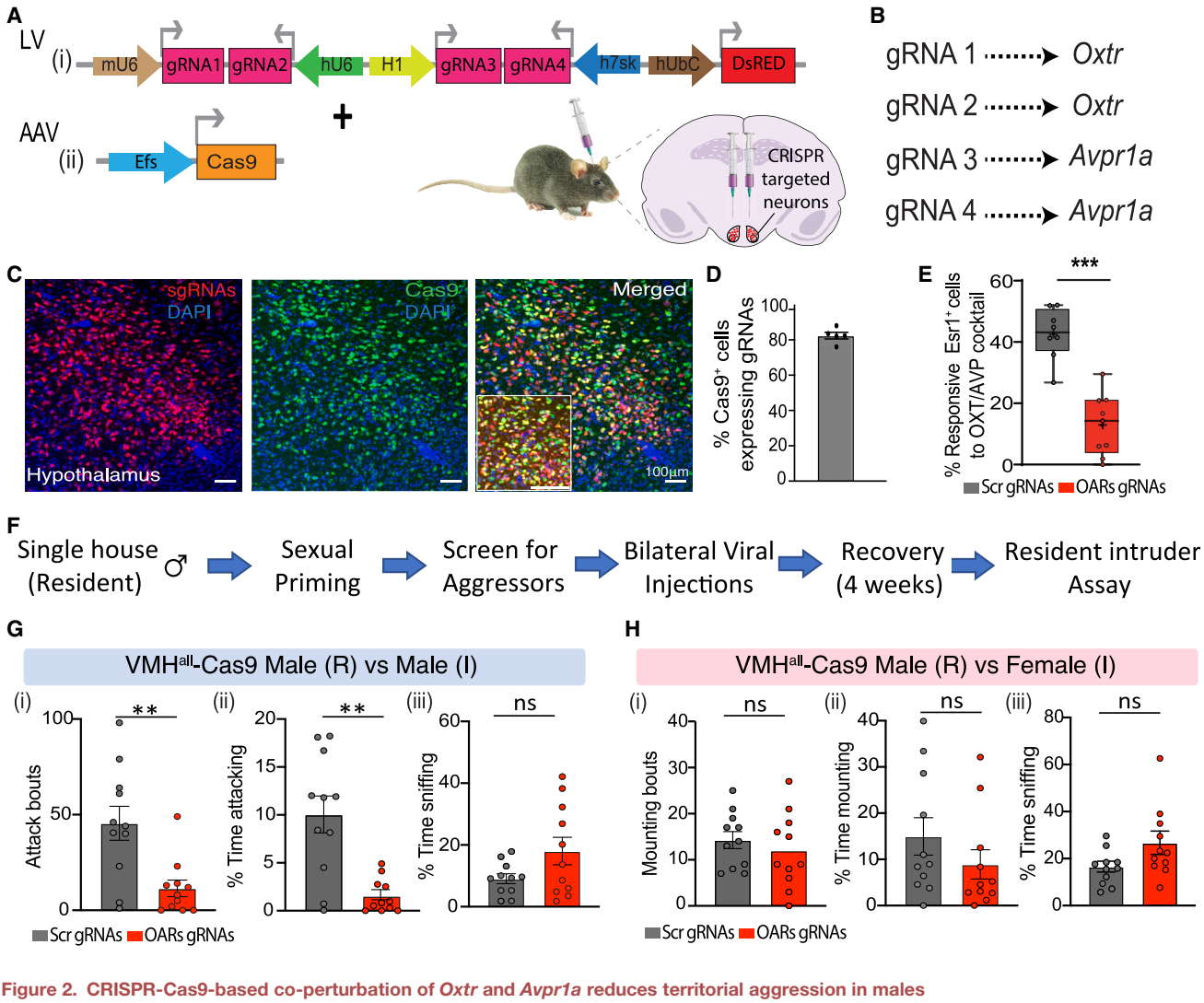

Figure 2. CRISPR-Cas9-based co-perturbation of *Oxtr* and *Avpr1a* reduces territorial aggression in males

(A) Schematic illustrating viral constructs for region-restricted multiplex CRISPR-Cas9 gene editing *in vivo*, using (i) a gRNA-dsRed LV and (ii) Cas9 AAV (see STAR Methods). Inset, males were co-injected bilaterally in VMH with the OAR gRNAs + Cas9 (experimental) or Scr gRNA + Cas9 (control) viral mixtures.

(B) Two different gRNAs each target *Oxtr* and *Avpr1a*.

(C) Immunostaining for dsRed (red) and Cas9 (green) in coronal VMH sections from co-injected animals. Sections are counterstained with DAPI (blue). Note high-magnification inset in "Merged" panel, lower left.

(D) Fraction of Cas9$^+$ cells expressing dsRed (gRNA virus); $n = 3$ mice.

(E) Fraction of Esr1$^+$ neurons responding to 400 nM AVP+ OXT in VMH slices from ESR1-2A-CRE mice co-injected with Cas9 AAV plus Cre-dependent OAR gRNAs-GCaMP8s or Scr-GCaMP8s AAVs (see Figure 3Ai). Datapoints represent brain slices. $n = 2$ Scr RNA (control) and $n = 3$ OARs (experimental) mice.

(F) Flow diagram illustrating experimental paradigm.

(G) Male-directed behaviors in experimental (red bars) and control (gray bars) males. $n = 11$ mice per group.

(H) Female-directed behaviors in experimental and control males. $n = 11$ mice per group.

Statistics: values plotted as mean ± SEM. $^{**}p \leq 0.01$, $^{***}p \leq 0.001$; Mann-Whitney test was performed in (E), (G), and (H).

See also Figure S2.

Altered VMHvl^{Esr1} neural activity during social interactions in mice with disrupted OXT and AVP receptors

Male VMHvl^{Esr1} neural activity normally increases during sniffing and attack toward an intruder male.[66,86] We therefore sought to analyze the activity of these neurons via calcium imaging in mice with or without co-disruption of *Oxtr* and *Avpr1a*. To restrict CRISPR-based gene editing to the same cell population that we wished to image, we constructed an AAV vector that encodes both the gRNAs and a Cre-dependent GCaMP8s[87] (Figure 3A, upper). In mice co-injected with a Cre-dependent Cas9 AAV, cells co-infected with both viruses are expected to undergo gene editing. The use of Cre-dependent AAVs in these experiments yields higher levels of expression than LVs as well as cell type specificity. Double-labeling with antibodies to GFP (GCaMP8s) and Cas9 in mice co-injected with the two

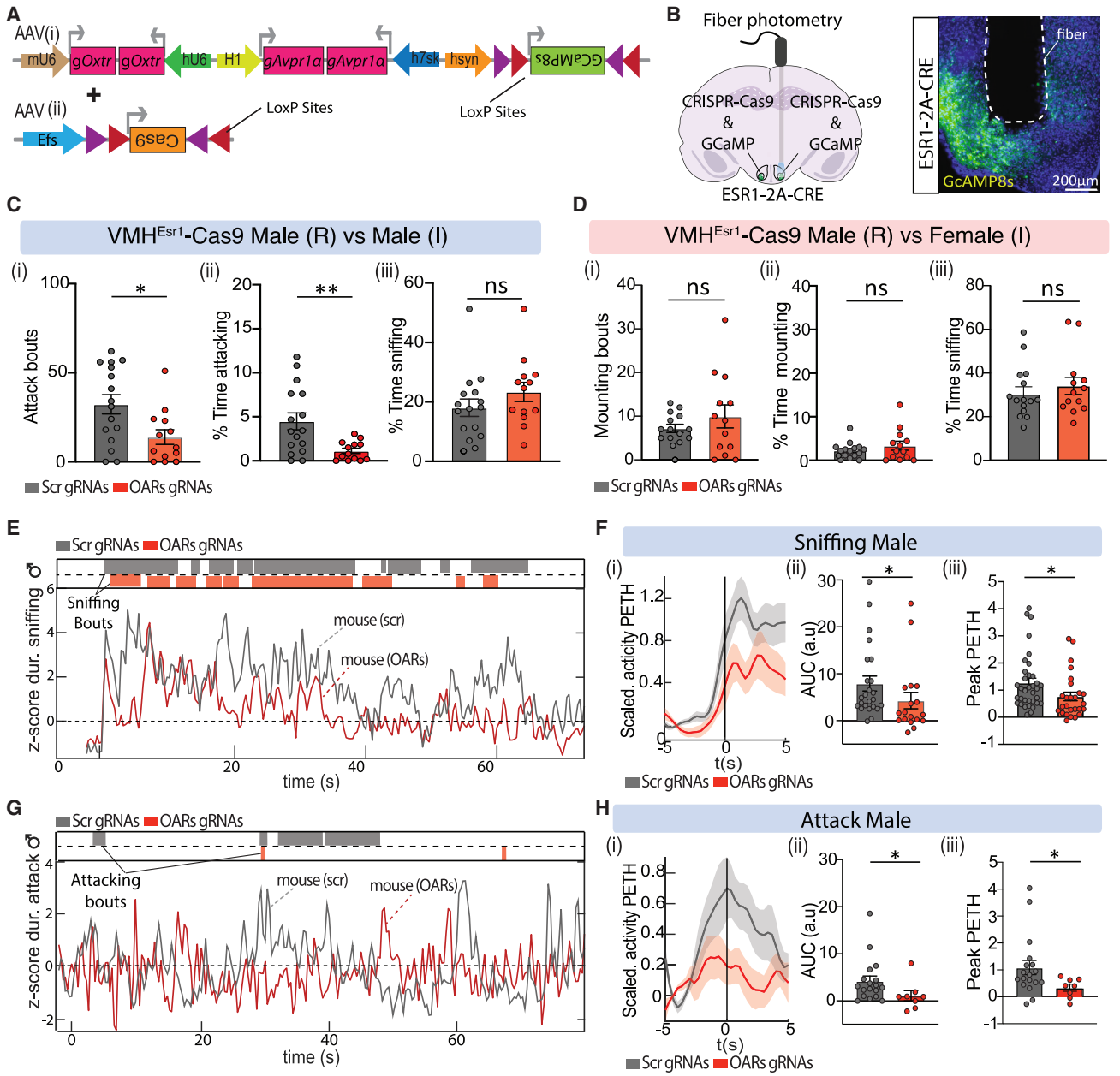

Figure 3. Co-disruption of OXT/AVP signaling alters VMHvlEsr1 bulk calcium activity

(A) Cre-dependent AAV constructs for combining multiplex CRISPR-Cas9 gene editing and calcium imaging *in vivo*.

(B) Left, schematic of experimental design combining bilateral gene editing of *Oxtr*/*Avpr1a* with unilateral fiber photometry. Right, GCaMP8s expression (green) in a coronal VMHvl section, counterstained with DAPI (blue).

(C) Male-directed behaviors in experimental and control males (n = 16 control and n = 13 experimental mice).

(D) Female-directed behaviors (n = 15 control and n = 13 experimental mice).

(E) Examples of fiber photometry traces from control (gray trace) and experimental (red trace) mice during male-directed sniffing bouts (behavior raster at top).

(F) Z scored behavior-triggered average (BTA) of bulk calcium activity in VMHvlEsr1 neurons during male-directed sniffing as a peri-event time histogram (PETH). (i) AUC (area under the curve) and (ii) peak PETH signal (first 1 min). Each datapoint represents a sniff bout. n = 5 mice per group.

(G) Examples of fiber photometry traces from control and experimental mice during attack.

(H) Z scored BTA of VMHvlEsr1 activity; (i) AUC and (ii) peak PETH during attack. n = 5 per group.

Statistics: values plotted as mean ± SEM. $^{*}p \leq 0.05$, $^{**}p \leq 0.01$, Mann-Whitney test was used in (C), (D), (F), and (H).

See also Figure S3.

Cre-dependent AAVs (Figure 3A) indicated that ~66% of GCaMP8s-expressing Esr1 neurons were Cas9$^+$ (Figures S3Ai and S3Aii).

As mentioned above, to verify the disruption of normal signaling responses to OXT and AVP in Esr1 neurons with co-targeting of *Oxtr* and *Avpr1a*, we performed *ex vivo* calcium imaging of VMH slices (Figure 1Fi) from ESR1-2A-CRE mice co-injected with the Cas9 and Cre-dependent gRNAs-GCaMP8s viruses (Figure 3Ai). The fraction of GCaMP8s-expressing cells responsive to mixed AVP and OXT peptides was reduced from 42.6% ± 3% in Scr gRNA controls to 13% ± 3.3% (~70% reduction) in *Oxtr/Avpr1a* gRNAs (Figure 2E). In addition, the few responsive cells in experimental slices were less activated by the peptides than cells in controls (Figure S3B). Thus, co-disruption of *Oxtr/Avpr1a* using our dual viral-based CRISPR-Cas9 system can reduce physiological responses to OXT and AVP in VMHvl^{Esr1} neurons, although they do not eliminate such responses completely.

We next used the Cre-dependent gene editing and GCaMP imaging systems to test whether *Oxtr/Avpr1a*-mediated signaling is required selectively in Esr1 neurons for aggressive behavior and to examine simultaneously how neural activity in these cells is affected. Bilateral co-disruption of *Oxtr/Avpr1a* in VMHvl^{Esr1} neurons significantly reduced most metrics of aggression toward male intruders compared with control mice, although to a somewhat lower extent than observed with the Cre-independent system (Figures 3Ci, 3Cii, and S3C). Using fiber photometry[88] to measure bulk calcium signals (Figure 3B), we observed a partial but statistically significant reduction in overall VMHvl^{Esr1} neuronal activity during the infrequent attack bouts exhibited by experimental mice (Figures 3G, compare red vs. gray rasters, and 3H). A reduction in VMHvl^{Esr1} activity during sniffing episodes was also observed in these mice (Figures 3E and 3F), even though the duration of sniffing behavior remained unaffected (Figure 3Ciii). By contrast, during male-female interactions, calcium signals in experimental males were not significantly different from controls (Figures S3E and S3F), consistent with the lack of an effect on mounting behavior (Figures 3D and S3D). Thus, males with bilateral co-disruption of Oxtr/Avpr1a-mediated signaling in VMHvl^{Esr1} neurons exhibited a reduction in both aggression and in Esr1$^+$ neural activity. However, these data did not distinguish whether the reduced activity was a cause or a consequence of the diminished aggressive behavior.

Single-cell CRISPRoscopy imaging of VMHvl^{Esr1} neurons with co-disruption of *Oxtr/Avpr1a*

To investigate how co-editing of *Oxtr/Avpr1a* affects activity in individual VMHvl^{Esr1} neurons, we imaged Ca^{2+} activity using a miniature head-mounted microscope[50] in Esr1-2A-CRE males co-injected with the experimental or control virus pairs. We call this approach CRISPRoscopy. To avoid reducing aggressive behavior, we performed calcium imaging and *Oxtr/Avpr1a* co-disruption unilaterally (Figure 4A). Because there are virtually no commissural connections between VMHvl, unilateral loss-of-function manipulations are typically compensated by the unmanipulated side.[70,86] Indeed, unilateral injected experimental animals displayed no deficits in sniffing or aggression compared with controls (Figure S4A). This design allowed us to determine the effects of *Oxtr/Avpr1a* co-disruption on neural activity and dynamics in behaviorally normal animals.

Effect of *Oxtr/Avpr1a* co-editing on VMHvl^{Esr1} activity and intruder sex representations

Our previous single-unit calcium imaging studies have shown that socially experienced males contain distinct VMHvl^{Esr1} subpopulations that are activated by male vs. female intruders, respectively.[66,70,86] This tuning separation was also clear in raster plots of VMHvl^{Esr1} units imaged in control vs. experimental (*Oxtr/Avpr1a* co-edited) males (Figure 4B). To quantify the proportion of intruder sex-"tuned" neurons, we measured unit activity during the first 1–2 min after the introduction of a male or female intruder in two ways: either by *Z* scoring (relative to the cell's mean fluorescence over the entire recording period) or by the change in fluorescence relative to the mean pre-intruder baseline[70,86] (in units of σ; see STAR Methods).

During interactions with a male intruder, the experimental cumulative distribution function (ECDF) and mean activity of all units (pooled from $n = 4$ control and $n = 7$ experimental animals) were slightly but significantly decreased in experimental mice (Figures 4Ei, 4Fi, and S4Di). However, the mean activity among cells considered as "active" ($\geq 2\sigma$ above baseline[66]) did not differ between control and experimental mice (Figure S4E). During interactions with females, there was no significant difference in activity (measured in σ above baseline) between experimental and control animals (Figures 4Eii and 4Fii), although *Z* scored activity showed a slight but significant increase (Figure S4Dii).

Next, we measured the percentage of male-selective (activity $\geq 2\sigma$ during male but not female interactions) and mixed-selectivity (activity $\geq 2\sigma$ during both male and female interactions) neurons within the Esr1$^+$ population during male-male interactions. The percentage of all male-activated neurons (selective or mixed) was slightly smaller in experimental than control mice (34.6% vs. 38.3%, respectively; Figures 4G and S4F), while there was a ~56% reduction in the small fraction of male-selective neurons (6.3% ± 2% vs. 14.4% ± 4%, respectively; Figures 4G and S4F). Conversely, during female interactions, the fraction of female-selective and mixed-selectivity neurons was increased by ~4% and ~44%, respectively, in experimental mice (Figures 4G and S4F). Together, these data are suggestive of a shift in sex-specific tuning from male-selective to mixed selectivity, a conclusion consistent with choice probability (CP) analysis (see below).

To determine whether this shift affected the ability to accurately decode intruder sex at the population level, we performed dimensionality reduction using partial least-squares (PLSs) regression. This analysis revealed a clear separation of responses during encounters with males vs. females in both control and experimental animals (Figures 4C and S4B). In addition, linear support vector machine (SVM) decoders trained on imaging data from either control or experimental mice correctly predicted intruder sex with virtually 100% accuracy (Figure 4D). Thus, in socially experienced animals, co-targeting of *Oxtr/Avpr1a* in VMHvl^{Esr1} cells does not disrupt the population coding of intruder sex,[66] despite the altered sex-selectivity of some of these units.

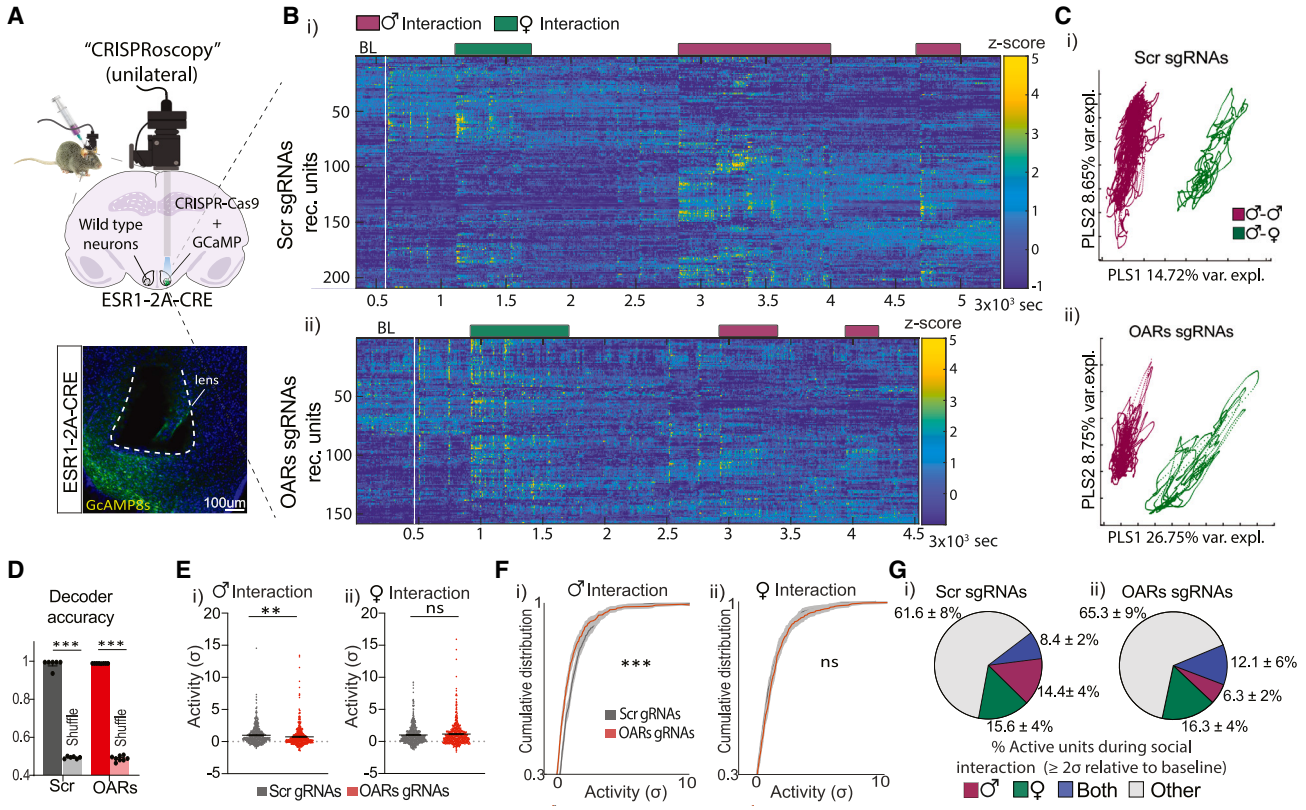

Figure 4. Single-cell imaging of VMHvl^{Esr1} neurons with co-disruption of *Oxtr/Avpr1a*

(A) Schematic of CRISPRoscopy. Upper, unilateral viral injection and microendoscope placement; lower, coronal VMHvl section illustrating GCaMP8s expression (green); blue, DAPI counterstain.

(B) Sample *Z* scored unit responses toward female and male intruders from control (i) and experimental (ii) male residents.

(C) VMHvl^{Esr1} ensemble representations of responses to intruder male (magenta trace) or female (green trace) for a control (i, Scr gRNAs) and experimental (ii, OARs gRNAs) male resident, projected onto a PLS regression against intruder sex. Axes indicate the percentage of variance explained for each PLS dimension.

(D) Accuracy of frame-wise decoders of intruder sex in control (Scr) and experimental (OARs) animals, trained on VMHvl^{Esr1} unit activity.

(E and F) Single-unit VMHvl^{Esr1} activity (E) and cumulative distribution of responses (F) in units of σ above pre-intruder baseline during 1 min of interaction.

(G) Percentage of male- or female-selective or co-active VMHvl^{Esr1} units (≥2σ above the pre-intruder baseline) in control (i) and experimental (ii) mice. $n = 5$ control, $n = 7$ experimental animals.

Statistics: values are means ± SEM. Mann-Whitney test was used in (D), and nested Mann-Whitney and Kolmogorov-Smirnov tests were performed in (E) and (F), respectively. $^{**}p \leq 0.01$, $^{***}p \leq 0.001$, $^{****}p \leq 0.0001$.

See also Figure S4.

Effect of *Oxtr/Avpr1a* co-editing on behavior representation in VMHvl during social encounters

Next, we examined the effect of co-disruption of *Oxtr/Avpr1a* on VMHvl^{Esr1} neuronal activity during the different behavioral phases of social interactions with males or females: appetitive (sniffing) or consummatory (attack or mounting, respectively). The ECDF and average single-unit activity during male-directed sniffing or attack were slightly but significantly lower in experimental than in control mice (Figures 5Ai, 5Aii, 5Ci, 5Cii, S5Ai, S5Bi, and S5Bii). By contrast, during social interactions with females, activity during sniffing and mounting was similar (Figures 5Aiii, 5Aiv, 5Ciii, 5Civ, S5Aii, S5Biii, and S5Biv). As an additional approach, we quantified the average activity in peri-event time histograms (PETHs) for each type of behavior (see STAR Methods). The mean activity during male-directed sniffing or attack was slightly but significantly lower in experimental than in control mice (Figures S5Ci and S5Cii), while it was significantly higher during female-directed sniffing but unchanged during mounting (Figures S5Ciii and S5Civ). In summary, the activity of VMHvl^{Esr1} units during different social behaviors was either unchanged or only modestly different between experimental and control animals, with statistically significant decreases or increases during male- vs. female-directed behaviors, respectively.

We next examined the proportion of behavior-selective active units (defined as units with activity ≥ 2σ above pre-intruder baseline during, e.g., sniff but not attack or vice versa).[66,70,86] As we previously showed, a relatively small fraction of VMHvl^{Esr1} neurons was selective for sniff or attack (~2.5%–10%), with the majority showing mixed behavioral selectivity (Figure 5B).[21,66,70,86] In experimental mice, during male interactions, the fraction of sniff-selective units was reduced by ~40% relative to controls (3.9% ± 2% in OARs gRNAs mice vs. 8.9% ± 3% in Scr gRNAs mice), while the small proportion

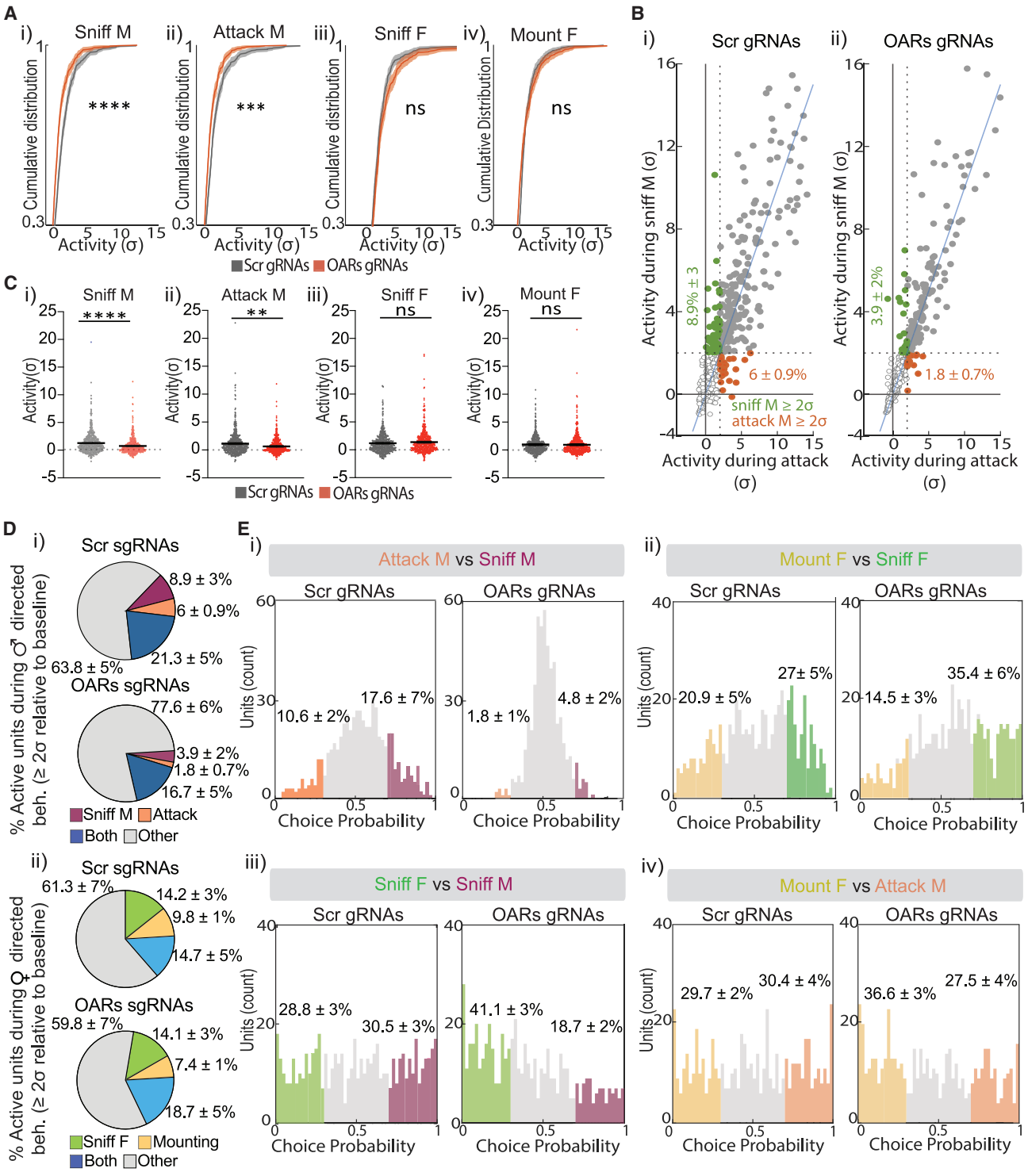

Figure 5. Activity and tuning of VMHvl^{Esr1} neurons with co-disruption of *Oxtr/Avpr1a* during social behaviors

(A) Cumulative distribution plots of VMHvl^{Esr1} activity (in units of σ relative to pre-intruder baseline) during male- (sniffing and attack) or female- (sniffing and mounting) directed behaviors in control (Scr gRNAs) and experimental (OARs gRNAs) mice.

(B) Scatter plots of single VMHvl^{Esr1} unit activity (σ above the pre-intruder baseline) during male-directed sniffing or attack in control and experimental mice. Green datapoints indicate sniff male (M)-selective units (≥ 2σ activity during male-directed sniffing and <2σ activity during attack); red datapoints depict attack male-selective units (≥2σ activity during attack and <2σ activity during sniffing).

(C) Average activity (σ) of single VMHvl^{Esr1} units during sniff or attack male (i and ii, M) or during sniff or mount female (iii and iv, F).

(legend continued on next page)

of attack-selective units was reduced by ~70% (1.8% ± 0.7% vs. 6% ± 0.9%; Figures 5B and 5Di). The fraction of neurons exhibiting mixed behavioral selectivity (i.e., active during both behaviors) was moderately reduced (~22%; Figure 5Di). Overall, there was a ~38% reduction in the fraction of active units during all male-directed behaviors (from 36.2% in control to 22.4% in experimental mice). By contrast, the fraction of female-directed sniffing- or mount-selective units was similar between control and experimental males (Figure 5Dii).

As an alternative metric of a cell's behavioral tuning, we calculated its CP: a cell was considered tuned to one of two pairwise-compared behaviors if it exhibited a CP > 0.7 that was significantly different ($p < 0.5$) from shuffled data.[66] We observed an ~80% and ~70% reduction in the percentage of attack- and sniff-tuned units, respectively, in experimental vs. control mice during male-male interactions (Figure 5Ei), with a concomitant ~18% increase in the fraction of units exhibiting mixed selectivity (CP for sniff vs. attack ≤ 0.7; Figures 5Ei, gray bars, and S5D). By contrast, the percentage of units tuned to sniffing females (vs. sniffing males) was increased in experimental mice (28.8% ± 3% vs. 41.1% ± 3%; Figure 5Eiii). We also observed a slight increase in the fraction of sniff female (vs. mount female)-tuned units and mount female (vs. attack male)-tuned units in experimental vs. control animals (Figure 5Eii). This analysis suggests that perturbation of normal OXTR/AVPR1a-mediated signaling decreases the relative number of units tuned to specific male-directed behaviors and increases the fraction of female behavior-tuned and mixed-selectivity cells.

Despite these shifts in behavior-selective tuning, there was no significant difference between control and experimental mice in the performance of linear decoders trained to distinguish attack from sniffing based on VMHvl^{Esr1} activity (Figure S5E). Thus, the population coding of social behavior by VMHvl^{Esr1} neurons[66] is unaffected by the co-disruption of *Oxtr/Avpr1a*.

VMHvl^{Esr1} line attractor dynamics require Oxtr/Avpr1a-mediated signaling

In addition to the level of activity and degree of feature- (behavior or sex)-specific tuning, neural dynamics can play an important role in the neural coding of cognitive function or internal state.[18] Using unsupervised linear dynamical systems modeling,[51,52] we recently discovered an approximate line attractor in VMHvl neural state space that encodes a low-dimensional, scalable representation of aggressiveness.[21] This line attractor is implemented by a subset of male-tuned VMHvl^{Esr1} neurons (~20%–25%) that are male-tuned and whose collective activity ramps up as social interactions escalate to attack and thereafter decays with a long (~100 s) time constant,[21] reflecting persistent activity in this subset. Since neuromodulatory signaling has been implicated in some forms of persistent neural activity,[28,89–91] we investigated whether line attractor dynamics during social behaviors are altered when OXTR/AVPR1a-mediated signaling is perturbed.

We fit recurrent switching linear dynamic system (rSLDS) models[52] individually to data from each experimental and control mouse, using data from animals with at least 31 imaged units. In both the control and experimental groups, the fit models reduced the dimensionality of the data to 5 latent factors and three states (S1–S3), capturing ~85% of the observed variance in neural activity. Model performance (cvR^2) was similar between control and experimental mice (Figure S6D). During male-male interactions, attack behavior occurred during a single rSLDS state in both control and experimental males. In control mice, the time constant (τ) of the 1st rSLDS dimension (derived from the first eigenvalue of the fit dynamics matrix; see STAR Methods) was significantly higher than that of the 2nd dimension (~100–120 s vs. ~40 s; Figures 6A and S6E). This yielded a line attractor score (calculated as the $\log_2$ of the ratio of the τ's of the 1st and 2nd dimensions) of ~1.6 (Figure 6F, gray bar), similar to that observed in mice without CRISPR-Cas9 gene editing.[21] By contrast, in experimental mice, the first two rSLDS dimensions had statistically indistinguishable τ values (<50 s; Figure 6C) due to a reduced 1st dimension τ (Figure S6E) and consequently a line attractor score close to zero (Figure 6F, red bar). However, during mounting behavior toward female intruders, co-perturbation of Oxtr/Avpr1a-mediated signaling did not significantly reduce the 1st dimension τ values or the line attractor score in experimental mice compared with controls (Figure S6F), consistent with the fact that most mating attractor-weighted neurons are female-tuned.[21]

To visualize neural dynamics in state space during male-male interactions, we generated 2D flow-field graphs spanned by the first two PCs of the rSLDS models. The flow fields are composed of arrows that indicate the rate and direction of change in neural population activity at different points in state space during social interactions (Figure S6C). The 2D flow field of control mice (Scr gRNAs) revealed a roughly linear region of low vector flow constituting the line attractor, along which the neural population vector progressed during an inter-male interaction (Figures 6Gi and S6Ci, dashed black lines). In a 3D dynamic landscape, where the length of the flow-field vectors at each position in neural state space is converted into the height of the landscape (and represented as a heat scale), in control animals, the population activity vector (PAV) progressed slowly along a trough-like structure (the line attractor) as aggression escalated (Figure 6Hi). By contrast, in experimental mice (OARs gRNAs), this line attractor was absent and was replaced by a point attractor (appearing as a circle in 2D and a cone in 3D), from which the PAV made "transient" excursions during bouts of sniffing or attack (Figures 6Gii, 6Hii, and S6Cii). This point attractor is called a "trivial" fixed point, corresponding to the resting state of a system in which population activity decays to a global minimum in the absence of inputs.

(D) Percentage of VMHvl^{Esr1} units active (defined as ≥2σ relative to pre-intruder baseline) during (i) male- or (ii) female-directed behaviors in control vs. experimental mice.

(E) Choice probability histograms of VMHvl^{Esr1} behavioral tuning during male- and female-directed behaviors in control (Scr gRNAs) and experimental (OARs gRNAs) mice. n = *5* control and *n* = 7 experimental mice.

Statistics: values plotted as means ± SEM. Nested Kolmogorov-Smirnov test was used in (A), nested Mann-Whitney test in (C). $^{**}p \leq 0.01$, $^{***}p \leq 0.001$, $^{****}p \leq 0.0001$.

See also Figure S5.

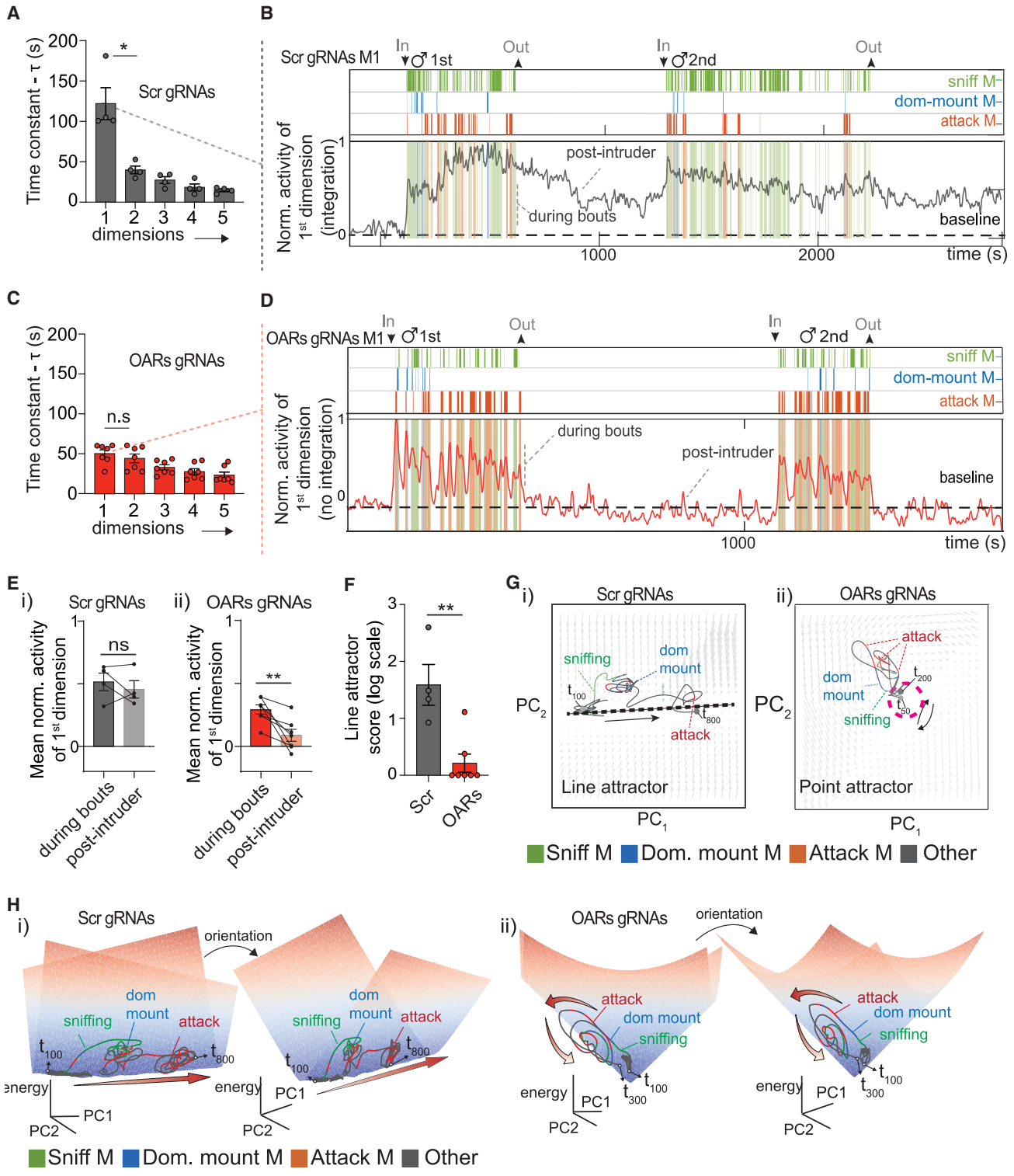

Figure 6. VMHvl^{Esr1} line attractor dynamics require Oxtr/Avpr1a-mediated signaling

(A and C) Time constants (τ) of all rSLDS dimensions, arranged in decreasing order in control (A) and experimental (C) mice.

(B and D) Normalized weighted average activity projections onto the time axis of the 1st dimension (integration dimension) for VMHvl^{Esr1} units in control (B) and experimental (D) M1 mice.

(E) Mean normalized VMHvl^{Esr1} 1st dimension activity during all behavioral bouts, or the post-intruder removal period, in control (i, $n = 4$) and experimental (ii, $n = 7$) mice.

(legend continued on next page)

This minimum (bottom of the cone in Figure 6Hii) represents the location of the PAV during baseline behavior in solitary mice. These data indicate that Oxtr/Avpr1a-mediated signaling is required for the emergence of line attractor dynamics in VMHvl during male-directed aggression but not during female-directed mounting.[21]

To investigate in more detail how co-disruption of *Oxtr/Avpr1a* perturbs VMHvl^{Esr1} attractor dynamics, we projected the weighted average of neuronal activity in the 1st rSLDS dimension (which generates the line attractor) onto the time axis and aligned it with behavior annotations. As reported previously,[21] in control mice, this activity ramped up during the progression from male-directed sniffing to attack, eventually reaching a plateau where it decayed slowly between attack bouts toward a single intruder and remained elevated between sequential trials with different intruders (Figures 6B, 6Ei, and S6A, "post-intruder"). By contrast, in experimental mice, 1st dimension neural activity decayed rapidly between attack bouts, displaying a "sawtooth" profile, and was significantly lower during the post-intruder (i.e., inter-trial) interval (Figures 6D, 6Eii, and S6B). The observation that 1st dimension activity in experimental mice is transiently elevated during aggressive episodes but does not remain stable across attack bouts and trials indicates that these neurons are still activated during attack but do not integrate recent activity in the same way as normal mice.

Oxtr/Avp1ra-mediating signaling controls VMHvl^{Esr1} persistent neural activity

We next investigated the dynamics of individual VMHvl^{Esr1} neurons caused by the co-disruption of *Oxtr/Avpr1a*. We focused initially on cells that were strongly weighted by the 1st rSLDS dimension (stem plots in Figure 7Aii). In raster plots from control mice, these units exhibited activity that persisted across inter-attack bout intervals and decayed slowly after removing the intruder male, visible as a "smearing" of rasters over time (Figure 7Ai, Scr gRNAs). By contrast, analogous units from experimental mice exhibited activity time-locked to attack bouts, visible as a vertical stripe-like pattern (Figure 7Ai, OAR gRNAs). To quantify these dynamics, we computed the average autocorrelation half-width (ACHW),[66] an approximate measure of the decay constant,[92,93] for each 1st dimension-weighted unit. The mean ACHW of these neurons across the entire social interaction was significantly shorter in experimental (9.86 ± 1 s) than in control mice (28.6 ± 1.23 s), by ~20 s (Figures 7Bi and S7A).

A reduction in the average ACHW was also observed among 2nd rSLDS dimension cells, as well as in the VMHvl^{Esr1} population as a whole (Figures 7Bii and 7C). However, the difference in mean ACHW between experimental and control animals was larger for 1st dimension-weighted units (~66%) than for 2nd dimension and total Esr1^{+} neurons (~61% and 50.9%, respectively). By contrast, the average and cumulative distribution of ACHWs among all VMHvl^{Esr1} neurons were only slightly reduced (by ~22%) during male-female interactions (Figure S7B). Thus, the decay time of individual VMHvl^{Esr1} units is faster, on average, in experimental than in control mice during male-male social interactions, especially among neurons that contribute to the 1st rSLDS dimension. This reduction in ACHW is consistent with the loss of line attractor dynamics caused by co-disruption of *Oxtr/Avpr1a* and may be a cause or a consequence of this loss.

OXT and AVP evoke persistent responses in VMHvl^{Esr1} neurons *ex vivo*

The observation that co-disruption of *Oxtr/Avpr1a* shortened the average decay time of Esr1^{+} units raised the question of whether adding these peptides to VMHvl would, conversely, lengthen this decay. Because it is not technically feasible to apply drugs or peptides directly at the site of microendoscope imaging, we utilized the *ex vivo* VMH brain slice preparation (Figure 1F). We imaged calcium activity in slices perfused with a cocktail of OXT + AVP and fitted an rSLDS model to the data (Figure S7C). This fit model captured 85% of the observed variance in neural activity. The time constant of dimension x1 (~90 s) was ~8- to 9-fold greater than that of x2 (~15 s; Figure S7D), similar to that observed *in vivo* (Figures 6A and 6C). Stem plots revealed that the neurons highly weighted by dimension x1 were distinct from those weighted by x2 (Figure S7E). Plotting the time-varying weighted average activity of x1 and x2 neurons revealed that the former exhibited slowly decaying responses to OXT + AVP application, while the latter exhibited more transient responses (Figures S7F–S7J). The two populations could also be identified independently of rSLDS analysis by quantifying the decay time of OXT + AVP-mediated VMHvl^{Esr1} population responses (Figure S7K). Interestingly, the inclusion of synaptic transmission blockers (20 μM CNQX and 10 μM MK-801) only slightly increased the decay rate during later phases of the peptide response (Figure S7L). Thus, persistent activity can be evoked by OXT + AVP in Esr1^{+} neurons within VMHvl slices *ex vivo*, suggesting that it does not require long-range interconnections with anatomically distant structures.

DISCUSSION

Using a novel approach that integrates CRISPR-Cas9 gene editing[48,49] with microendoscope imaging[50] and dynamical systems analysis,[51,52] we show that OXT and/or AVP receptors are required for persistent neural activity, line attractor dynamics, and aggression in VMHvl^{Esr1} neurons[64,70,71] (Figure 7D). These

(F) Line attractor scores for VMHvl^{Esr1} population activity in control (n = 4) and experimental (n = 7) mice.
(G) Inferred flow fields of fit rSLDS models for VMHvl^{Esr1} neuronal activity, reduced to the first 2 principal components (PCs), from control (i) and experimental (ii) mice M1 with projected neural trajectories (traces) and behavior annotations (color labels).
(H) Inferred 3D dynamic landscape of fit rSLDS model in VMHvl control mouse M1 (i) and experimental mouse M1 (ii). Different views of line (i) and point attractors (ii) are shown. Red arrows (i) depict movement along line attractor. All sniffing, dominance mounting, and attack bouts toward an intruder male are depicted in the behavioral rasters in (B) and (D).
Statistics: values plotted as means ± SEM. Kruskal-Wallis test was performed in (A) and (C). Paired t test was performed in (E) and Mann-Whitney test in (F) *$p \leq 0.05$, **$p \leq 0.01$.
See also Figure S6.

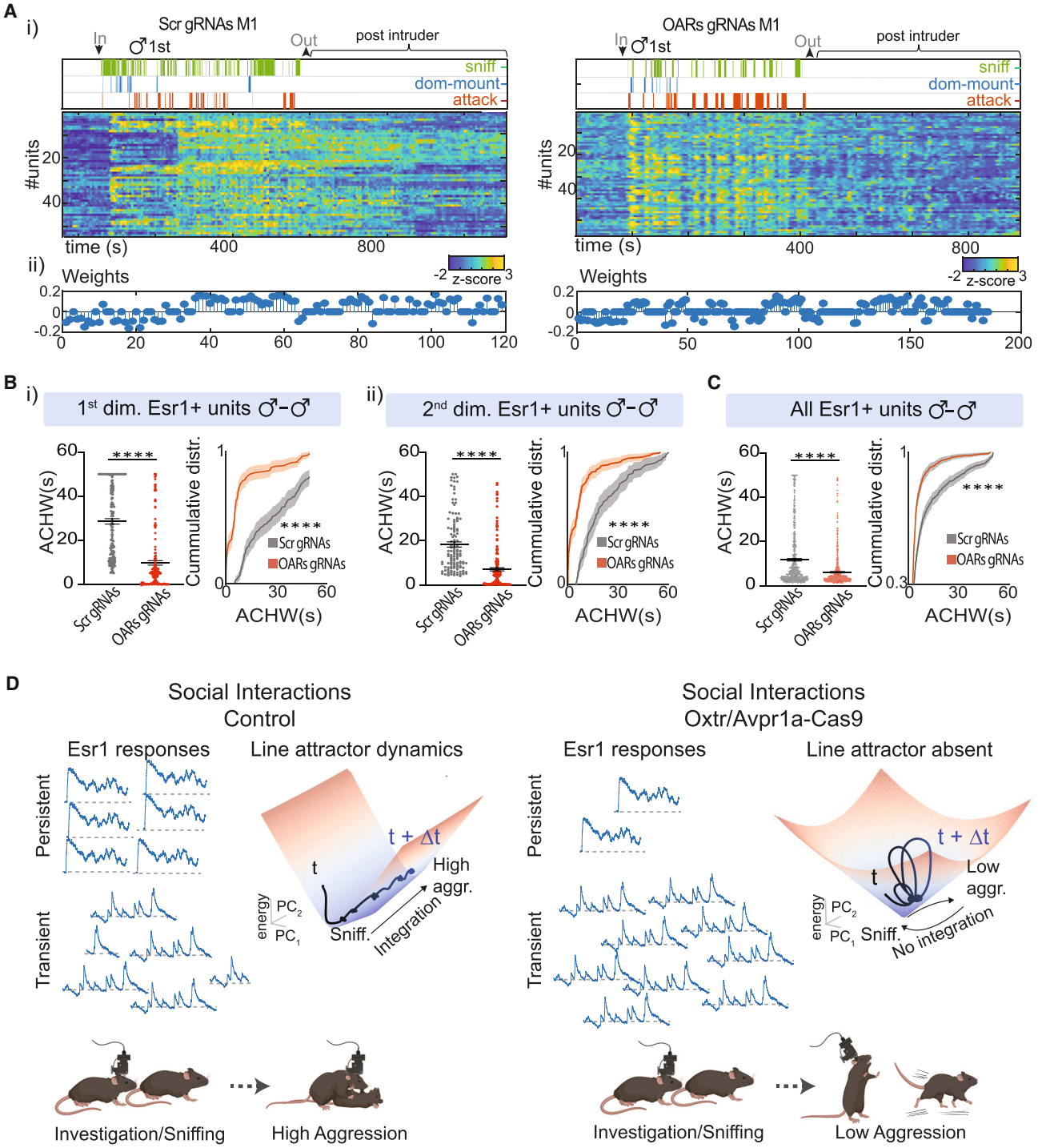

Figure 7. Oxtr/Avp1ra-mediating signaling modulates VMHvl^{Esr1} persistent neural activity

(A) (i) Behavioral raster plots and the corresponding neural activity rasters (*Z* scored) of individual VMHvl^{Esr1} units weighted on the 1st dimension in representative control (left) and experimental (right) M1 mice. (ii) Absolute rSLDS weights of neurons contributing to the 1st dimension are shown as stem plots. See Figure S6 for additional mice.

(B) Average single-unit and cumulative distribution of neuronal persistence measured by ACHW of individual VMHvl^{Esr1} units weighted on the 1st dimension (i) and the 2nd dimension (ii) during the entire duration of male-male interactions. n = 4 control, n = 7 experimental animals.

(C) As in (B), except data from all Esr1^{+} units during the first 1–2 min of male-male interactions. n = 5 control, n = 7 experimental animals.

(legend continued on next page)

results in turn suggest that neuropeptides may control certain behaviors, at least in part, through an influence on population neural dynamics. Our approach should help unify molecular and circuit-level approaches with "manifold"-level approaches[13,14,23] to understanding the neural control of behavior, emotion, and cognition.

The impact of Oxtr/Avpr1a co-disruption on VMHvl^{Esr1} activity, tuning, and dynamics

In principle, the observed reduction in aggression could be a consequence of reduced activity of VMHvl^{Esr1} neurons. Indeed, fiber photometry and CRISPRoscopy revealed a partial but statistically significant decrease in average activity during sniffing or attacking males. The percentage of attack- and sniff-tuned cells was also partially but significantly reduced. These relatively modest effects, however, seem unlikely to account for the strong reduction in aggressiveness caused by bilateral disruption of *Oxtr* and *Avpr1a*. Nevertheless, as aggression requires a high level of VMHvl^{Esr1} activity,[64,86] we cannot exclude that these effects on activity level and tuning contribute to the behavioral phenotype. By contrast, co-disruption of *Oxtr*/*Avpr1a* caused a virtually complete elimination of the line attractor. Consistent with this finding, the average ACHW of VMHvl^{Esr1} neurons weighted on the integration (1st) dimension was strongly reduced. These results suggest that the reduced aggression may be due, at least in part, to the loss of the line attractor. However, more specific perturbations will be required to test decisively whether selective elimination of line attractor dynamics affects aggression.

How co-disruption of *Oxtr*/*Avpr1a* eliminates the line attractor is not clear. Our between-subject comparisons do not allow us to distinguish whether the reduced ACHW reflects a change in the dynamics of individual cells or the inactivation of a subset of cells with long decay time constants. However, persistent calcium responses evoked by bath application of OXT + AVP to VMHvl^{Esr1} neurons *ex vivo* were strongly reduced by co-disruption of *Oxtr*/*Avpr1a*. Persistent activity induced by OXT *ex vivo* has been demonstrated in hippocampal neurons.[91]

Notably, only a slight reduction in persistence was observed for VMHvl^{Esr1} units that were active during male-female interactions. These female-tuned units are largely distinct from the units active during male-male interactions.[66,86] Consistent with this, a line attractor observed during male mounting of females[21] was not perturbed by co-editing of *Oxtr* and *Avpr1a*, and there was no deficit in male-female mating behavior. Together, these data argue that the effect of the *Oxtr*/*Avpr1a* perturbation on neural dynamics is unlikely due to indiscriminate changes in VMH cytoarchitecture or function.

A line attractor dependent on neuropeptide signaling

Most theoretical studies have assumed that attractor dynamics emerge from recurrent fast synaptic connectivity,[17–19] as seen in the *Drosophila* ring attractor system.[24,29] Our finding that neuropeptide signaling is required for line attractor dynamics and persistent activity is consistent with recurrent neural network (RNN) modeling of persistent activity in VMH circuits, which indicated that only models incorporating both recurrence and slow neuromodulation were accounted for in the experimental observations.[12,65] OXT can cause increased excitability in anterior VMHvl neurons,[69] and it could also strengthen recurrent connectivity within this nucleus[12,94] or between interconnected regions.[95] We emphasize, however, that neither *Oxt* nor *Avp* mRNAs are synthesized by VMHvl^{Esr1} neurons[68]; therefore, their source(s) must be extrinsic to this nucleus.[69]

A role for neuropeptides in implementing slow attractor dynamics that control innate behaviors is appealing for several reasons. First, it may overcome the dependence of purely glutamatergic attractor networks on fine-tuned synaptic connectivity.[17,18,27] This requirement for fine-tuning makes attractors very "fragile," i.e., highly sensitive to experimental or physiological disruption (but see Koulakov et al.[96] and Goldman et al.[97]). RNN modeling has indicated that VMHvl networks incorporating slow neuromodulatory transmission can reproduce observed network time constants over a much wider range of synaptic connectivity densities than purely glutamatergic networks,[65] suggesting that neuropeptidergic based line attractors may be less dependent on precise patterns of synaptic connectivity. Second, neuropeptidergic signaling can yield decay constants on the timescale of 100 s of seconds. Although sufficiently fine-tuned glutamatergic attractor networks can in theory persist indefinitely,[18] persistent activity in other experimentally described attractors has typically been observed for just a few seconds,[19,98] making it unclear if they can sustain activity on longer timescales. Finally, slow dynamics may be better suited to encode long-lasting and escalating affective states, such as aggressiveness, than the attractors invoked to compute functions like gaze stabilization,[17] working memory,[98] and head direction.[24]

Neuropeptides may be also be advantageous for implementing line attractors or leaky integrators because their expression can be modulated by hormones[99] and neural activity.[100] For example, longitudinal single-cell calcium imaging studies from a female-specific VMHvl subpopulation that controls sexual receptivity[20,101,102] have revealed an estrus cycle-dependent line attractor.[20] Finally, neuropeptide receptor expression is more restricted than that of receptors for biogenic amines.[103] This specificity could allow the regulation of different (and potentially competing) attractors within a local network[21] by distinct neuropeptides.

The results described demonstrate how the power of multiplex gene editing technology[48,49] can combined with single-cell imaging to identify mechanisms that implement attractor dynamics.[18] They also suggest that population neural dynamics

(D) Schematic of working model. Oxtr and Avpr1a-mediated signaling controls aggression escalation by regulating VMHvl^{Esr1} single-cell dynamics (transient and persistent activity) and line attractor dynamics (left) during male-male interactions. Co-disruption of *Oxtr* and *Avpr1a* causes reduced persistent and increased transient responses, the absence of the line attractor (replaced by a trivial point attractor), and reduced aggression (right).

Statistics: values plotted as mean ± SEM. Nested Mann-Whitney test was performed for (Bi), (Ci), and (Aii inset). Kolmogorov test was performed (Aii), (Bii), and (Cii) ****$p \leq 0.0001$.

See also Figure S7.

may mediate the behavioral functions of some neuropeptides.[38,40] In this way, this approach may enable mechanistic explanations in neuroscience that unify different levels of abstraction and of biological organization.[23]

Limitations of the study

A technical limitation of our approach is that two different viruses were used to deliver gRNAs-GCaMP and Cas9. Consequently, not all GCaMP$^+$ cells captured in our imaging analysis are necessarily Cas9$^+$ (and therefore mutant for *Oxtr*/*Avpr1*). Our data indicate co-infection rates of ~65%–80% at the injection site, depending on the viruses used. We also lack an accurate estimation of the fraction of cells exhibiting homozygous INDELs in the *Oxtr* and *Avpr1a* genes *in vivo*. Another limitation is our reliance on between-subject comparisons of experimental vs. control mice. Our rSLDS analysis showed that there was no effect of *Oxtr*/*Avpr1a* co-editing on male mounting of females but do not exclude a possible effect on intromission. Finally, our results do not distinguish the individual roles of OXTR and AVPR1a, nor do they establish the cellular source and release dynamics of the endogenous peptide(s) that activate these receptors *in vivo* during aggression. Further studies will be required to elucidate these biologically important details.

STAR★METHODS

Detailed methods are provided in the online version of this paper and include the following:

- KEY RESOURCES TABLE
- RESOURCE AVAILABILITY
  - Lead contact
  - Materials availability
  - Data and code availability
- EXPERIMENTAL MODEL AND STUDY PARTICIPANT DETAILS
  - Viruses
- METHOD DETAILS
  - Generation of multiplex CRISPR/*Streptococcus pyogenes* Cas9 vectors
  - Generation of Neuro2A constitutively expressed CAS9 cells and screening of gRNAs
  - Screening for aggressor male and resident intruder assay
  - Acute brain slices preparation
  - Peptide perfusion and two-photon calcium imaging experiments
  - Behavior recording
  - Behavior annotations
  - Stereotaxic surgery
  - Histology
  - Fiberphotometry recordings
  - Microendoscope recordings
  - Microendoscope data extraction
- QUANTIFICATION AND STATISTICAL ANALYSIS
  - Transcriptomic analysis of *Esr1*, *Oxtr*, *Avpr1a* mRNAs
  - Fiberphotometry analysis
  - Microendoscope neural data analysis
  - Dimensionality reduction for visualizing intruder sex
  - Decoding intruder sex from neural data
  - Decoding behavior from neural activity
  - Statistical analysis
  - Dynamical system models of neural data
  - Visualization of attractor dynamics as 3D landscape
  - Estimation of time constants & calculation of line attractor score

ACKNOWLEDGMENTS

We thank H. Inagaki, A. Kennedy, B. Weissbourd, and M. Schnitzer for comments on this manuscript; C. Chiu for laboratory management; G. Mancuso and L. Chavarria for administrative assistance; and members of the Anderson lab for helpful comments on this project. We also thank Y. Li, L. Geng, and H. Wang for sharing their OXT-GRAB sensor in advance of publication. G.M. has been supported by post-doctoral fellowships from the Tianqio and Chrissy Chen Institute for Neuroscience, the Helen Hay Whitney Foundation, and the Della Martin Foundation. A.N. is supported by a National Science Scholarship from the Agency of Science, Technology, and Research, Singapore. This work was supported in part by NIH grants NS123916, MH1223612, and MH070053. D.J.A. is an Investigator of the Howard Hughes Medical Institute. The content of this paper is solely the responsibility of the authors and does not necessarily represent the official views of the National Institutes of Health. We support inclusive, diverse, and equitable conduct of research. We acknowledge that this research was conducted at Caltech, which is located on the unceded land of the Indigenous Tongva people.

AUTHOR CONTRIBUTIONS

G.M. and D.J.A. conceived the project. G.M. and D.J.A. wrote and prepared the manuscript with input from A.N. G.M. performed all the experiments, with help from B.Y. for microendoscope imaging or from D.-W.K. and S.K. for two-photon slice imaging experiments. A.V. participated in the revision phase of the manuscript. G.M. and A.N. performed quantitative measurements of behavior and microendoscope imaging data. A.N., under the supervision of S.W.L., performed the dynamical system modeling and decoder analyses.

DECLARATION OF INTERESTS

The authors declare no competing interests.

Received: September 25, 2023
Revised: June 23, 2024
Accepted: August 7, 2024
Published: August 27, 2024

REFERENCES

1. Sternson, S.M. (2013). Hypothalamic survival circuits: blueprints for purposive behaviors. Neuron *77*, 810–824. https://doi.org/10.1016/j.neuron.2013.02.018.
2. Anderson, D.J., and Adolphs, R. (2014). A framework for studying emotions across species. Cell *157*, 187–200. https://doi.org/10.1016/j.cell.2014.03.003.
3. Zych, A.D., and Gogolla, N. (2021). Expressions of emotions across species. Curr. Opin. Neurobiol. *68*, 57–66. https://doi.org/10.1016/j.conb.2021.01.003.
4. Damasio, A., and Carvalho, G.B. (2013). The nature of feelings: evolutionary and neurobiological origins. Nat. Rev. Neurosci. *14*, 143–152. https://doi.org/10.1038/nrn3403.
5. Dolan, R.J. (2002). Emotion, cognition, and behavior. Science *298*, 1191–1194. https://doi.org/10.1126/science.1076358.
6. Flavell, S.W., Gogolla, N., Lovett-Barron, M., and Zelikowsky, M. (2022). The emergence and influence of internal states. Neuron *110*, 2545–2570. https://doi.org/10.1016/j.neuron.2022.04.030.
7. Malezieux, M., Klein, A.S., and Gogolla, N. (2023). Neural Circuits for Emotion. Annu. Rev. Neurosci. *46*, 211–231. https://doi.org/10.1146/annurev-neuro-111020-103314.
8. Luo, L., Callaway, E.M., and Svoboda, K. (2018). Genetic Dissection of Neural Circuits: A Decade of Progress. Neuron *98*, 256–281. https://doi.org/10.1016/j.neuron.2018.03.040.
9. Deisseroth, K. (2014). Circuit dynamics of adaptive and maladaptive behaviour. Nature *505*, 309–317. https://doi.org/10.1038/nature12982.

10. Xu, S., Yang, H., Menon, V., Lemire, A.L., Wang, L., Henry, F.E., Turaga, S.C., and Sternson, S.M. (2020). Behavioral state coding by molecularly defined paraventricular hypothalamic cell type ensembles. Science *370*, eabb2494. https://doi.org/10.1126/science.abb2494.

11. Augustine, V., Lee, S., and Oka, Y. (2020). Neural Control and Modulation of Thirst, Sodium Appetite, and Hunger. Cell *180*, 25–32. https://doi.org/10.1016/j.cell.2019.11.040.

12. Kennedy, A., Kunwar, P.S., Li, L.Y., Stagkourakis, S., Wagenaar, D.A., and Anderson, D.J. (2020). Stimulus-specific hypothalamic encoding of a persistent defensive state. Nature *586*, 730–734. https://doi.org/10.1038/s41586-020-2728-4.

13. Jazayeri, M., and Afraz, A. (2017). Navigating the Neural Space in Search of the Neural Code. Neuron *93*, 1003–1014. https://doi.org/10.1016/j.neuron.2017.02.019.

14. Ebitz, R.B., and Hayden, B.Y. (2021). The population doctrine in cognitive neuroscience. Neuron *109*, 3055–3068. https://doi.org/10.1016/j.neuron.2021.07.011.

15. Shenoy, K.V., Sahani, M., and Churchland, M.M. (2013). Cortical control of arm movements: a dynamical systems perspective. Annu. Rev. Neurosci. *36*, 337–359. https://doi.org/10.1146/annurev-neuro-062111-150509.

16. Mante, V., Sussillo, D., Shenoy, K.V., and Newsome, W.T. (2013). Context-dependent computation by recurrent dynamics in prefrontal cortex. Nature *503*, 78–84. https://doi.org/10.1038/nature12742.

17. Seung, H.S. (1996). How the brain keeps the eyes still. Proc. Natl. Acad. Sci. USA *93*, 13339–13344. https://doi.org/10.1073/pnas.93.23.13339.

18. Khona, M., and Fiete, I.R. (2022). Attractor and integrator networks in the brain. Nat. Rev. Neurosci. *23*, 744–766. https://doi.org/10.1038/s41583-022-00642-0.

19. Inagaki, H.K., Chen, S., Daie, K., Finkelstein, A., Fontolan, L., Romani, S., and Svoboda, K. (2022). Neural Algorithms and Circuits for Motor Planning. Annu. Rev. Neurosci. *45*, 249–271. https://doi.org/10.1146/annurev-neuro-092021-121730.

20. Liu, M., Nair, A., Coria, N., Linderman, S.W., and Anderson, D.J. (2024). Encoding of female mating dynamics by a hypothalamic line attractor. Nature. https://doi.org/10.1038/s41586-024-07916-w.

21. Nair, A., Karigo, T., Yang, B., Ganguli, S., Schnitzer, M.J., Linderman, S.W., Anderson, D.J., and Kennedy, A. (2023). An approximate line attractor in the hypothalamus encodes an aggressive state. Cell *186*, 178–193.e15. https://doi.org/10.1016/j.cell.2022.11.027.

22. Sylwestrak, E.L., Jo, Y., Vesuna, S., Wang, X., Holcomb, B., Tien, R.H., Kim, D.K., Fenno, L., Ramakrishnan, C., Allen, W.E., et al. (2022). Cell-type-specific population dynamics of diverse reward computations. Cell *185*, 3568–3587.e27. https://doi.org/10.1016/j.cell.2022.08.019.

23. Langdon, C., Genkin, M., and Engel, T.A. (2023). A unifying perspective on neural manifolds and circuits for cognition. Nat. Rev. Neurosci. *24*, 363–377. https://doi.org/10.1038/s41583-023-00693-x.

24. Hulse, B.K., and Jayaraman, V. (2020). Mechanisms underlying the neural computation of head direction. Annu. Rev. Neurosci. *43*, 31–54. https://doi.org/10.1146/annurev-neuro-072116-031516.

25. Kim, S.S., Rouault, H., Druckmann, S., and Jayaraman, V. (2017). Ring attractor dynamics in the Drosophila central brain. Science *356*, 849–853. https://doi.org/10.1126/science.aal4835.

26. Inagaki, H.K., Chen, S., Ridder, M.C., Sah, P., Li, N., Yang, Z., Hasanbegovic, H., Gao, Z., Gerfen, C.R., and Svoboda, K. (2022). A midbrain-thalamus-cortex circuit reorganizes cortical dynamics to initiate movement. Cell *185*, 1065–1081.e23. https://doi.org/10.1016/j.cell.2022.02.006.

27. Goldman, M., Compte, A., and Wang, X.-J. (2007). Neural integrators: recurrent mechanisms and models. New Encyclopedia of Neuroscience, 1–26.

28. Major, G., and Tank, D. (2004). Persistent neural activity: prevalence and mechanisms. Curr. Opin. Neurobiol. *14*, 675–684. https://doi.org/10.1016/j.conb.2004.10.017.

29. Turner-Evans, D.B., Jensen, K.T., Ali, S., Paterson, T., Sheridan, A., Ray, R.P., Wolff, T., Lauritzen, J.S., Rubin, G.M., Bock, D.D., and Jayaraman, V. (2020). The Neuroanatomical Ultrastructure and Function of a Biological Ring Attractor. Neuron *108*, 145–163.e10. https://doi.org/10.1016/j.neuron.2020.08.006.

30. Hökfelt, T., Broberger, C., Xu, Z.Q., Sergeyev, V., Ubink, R., and Diez, M. (2000). Neuropeptides–an overview. Neuropharmacology *39*, 1337–1356. https://doi.org/10.1016/s0028-3908(00)00010-1.

31. Russo, A.F. (2017). Overview of Neuropeptides: Awakening the Senses? Headache *57*, 37–46. suppl 2. https://doi.org/10.1111/head.13084.

32. Wang, P., Wang, S.C., Liu, X., Jia, S., Wang, X., Li, T., Yu, J., Parpura, V., and Wang, Y.F. (2022). Neural Functions of Hypothalamic Oxytocin and its Regulation. ASN Neuro *14*, 17590914221100706. https://doi.org/10.1177/17590914221100706.

33. Koppan, M., Nagy, Z., Bosnyak, I., and Reglodi, D. (2022). Female reproductive functions of the neuropeptide PACAP. Front. Endocrinol. (Lausanne) *13*, 982551. https://doi.org/10.3389/fendo.2022.982551.

34. Asahina, K., Watanabe, K., Duistermars, B.J., Hoopfer, E., González, C.R., Eyjólfsdóttir, E.A., Perona, P., and Anderson, D.J. (2014). Tachykinin-Expressing Neurons Control Male-Specific Aggressive Arousal in Drosophila. Cell *156*, 221–235. https://doi.org/10.1016/j.cell.2013.11.045.

35. Siegel, A., Roeling, T.A., Gregg, T.R., and Kruk, M.R. (1999). Neuropharmacology of brain-stimulation-evoked aggression. Neurosci. Biobehav. Rev. *23*, 359–389. https://doi.org/10.1016/s0149-7634(98)00040-2.

36. Zelikowsky, M., Hui, M., Karigo, T., Choe, A., Yang, B., Blanco, M.R., Beadle, K., Gradinaru, V., Deverman, B.E., and Anderson, D.J. (2018). The Neuropeptide Tac2 Controls a Distributed Brain State Induced by Chronic Social Isolation Stress. Cell *173*, 1265–1279.e19. https://doi.org/10.1016/j.cell.2018.03.037.

37. Lim, M.M., and Young, L.J. (2006). Neuropeptidergic regulation of affiliative behavior and social bonding in animals. Horm. Behav. *50*, 506–517. https://doi.org/10.1016/j.yhbeh.2006.06.028.

38. Marder, E. (2012). Neuromodulation of neuronal circuits: back to the future. Neuron *76*, 1–11. https://doi.org/10.1016/j.neuron.2012.09.010.

39. Nusbaum, M.P., Blitz, D.M., and Marder, E. (2017). Functional consequences of neuropeptide and small-molecule co-transmission. Nat. Rev. Neurosci. *18*, 389–403. https://doi.org/10.1038/nrn.2017.56.

40. Bargmann, C.I., and Marder, E. (2013). From the connectome to brain function. Nat. Methods *10*, 483–490. https://doi.org/10.1038/nmeth.2451.

41. Flavell, S.W., Pokala, N., Macosko, E.Z., Albrecht, D.R., Larsch, J., and Bargmann, C.I. (2013). Serotonin and the neuropeptide PDF initiate and extend opposing behavioral states in C. elegans. Cell *154*, 1023–1035. https://doi.org/10.1016/j.cell.2013.08.001.

42. Ji, N., Madan, G.K., Fabre, G.I., Dayan, A., Baker, C.M., Kramer, T.S., Nwabudike, I., and Flavell, S.W. (2021). A neural circuit for flexible control of persistent behavioral states. eLife *10*, e62889. https://doi.org/10.7554/eLife.62889.

43. Kato, S., Kaplan, H.S., Schrödel, T., Skora, S., Lindsay, T.H., Yemini, E., Lockery, S., and Zimmer, M. (2015). Global Brain Dynamics Embed the Motor Command Sequence of Caenorhabditis elegans. Cell *163*, 656–669. https://doi.org/10.1016/j.cell.2015.09.034.

44. Dag, U., Nwabudike, I., Kang, D., Gomes, M.A., Kim, J., Atanas, A.A., Bueno, E., Estrem, C., Pugliese, S., Wang, Z., et al. (2023). Dissecting the functional organization of the C. elegans serotonergic system at whole-brain scale. Cell *186*, 2574–2592.e20. https://doi.org/10.1016/j.cell.2023.04.023.

45. Root, C.M., Ko, K.I., Jafari, A., and Wang, J.W. (2011). Presynaptic facilitation by neuropeptide signaling mediates odor-driven food search. Cell *145*, 133–144. https://doi.org/10.1016/j.cell.2011.02.008.

46. Watanabe, K., Chiu, H., Pfeiffer, B.D., Wong, A.M., Hoopfer, E.D., Rubin, G.M., and Anderson, D.J. (2017). A Circuit Node that Integrates

Convergent Input from Neuromodulatory and Social Behavior-Promoting Neurons to Control Aggression in Drosophila. Neuron *95*, 1112–1128.e7. https://doi.org/10.1016/j.neuron.2017.08.017.

47. Andalman, A.S., Burns, V.M., Lovett-Barron, M., Broxton, M., Poole, B., Yang, S.J., Grosenick, L., Lerner, T.N., Chen, R., Benster, T., et al. (2019). Neuronal Dynamics Regulating Brain and Behavioral State Transitions. Cell *177*, 970–985.e20. https://doi.org/10.1016/j.cell.2019.02.037.
48. Heidenreich, M., and Zhang, F. (2016). Applications of CRISPR-Cas systems in neuroscience. Nat. Rev. Neurosci. *17*, 36–44. https://doi.org/10.1038/nrn.2015.2.
49. Doudna, J.A., and Charpentier, E. (2014). Genome editing. The new frontier of genome engineering with CRISPR-Cas9. Science *346*, 1258096. https://doi.org/10.1126/science.1258096.
50. Ziv, Y., Burns, L.D., Cocker, E.D., Hamel, E.O., Ghosh, K.K., Kitch, L.J., El Gamal, A., and Schnitzer, M.J. (2013). Long-term dynamics of CA1 hippocampal place codes. Nat. Neurosci. *16*, 264–266. https://doi.org/10.1038/nn.3329.
51. Glaser, J., Whiteway, M., Cunningham, J.P., Paninski, L., and Linderman, S. (2020). Recurrent switching dynamical systems models for multiple interacting neural populations. Advances in neural information processing systems *33*, 14867–14878.
52. Linderman, S., Johnson, M., Miller, A., Adams, R., Blei, D., and Paninski, L. (2017). Bayesian learning and inference in recurrent switching linear dynamical systems. In Proceedings of the 20th International Conference on Artificial Intelligence and Statistics, pp. 914–922.
53. Zha, X., and Xu, X.H. (2021). Neural circuit mechanisms that govern intermale attack in mice. Cell. Mol. Life Sci. *78*, 7289–7307. https://doi.org/10.1007/s00018-021-03956-x.
54. Hashikawa, Y., Hashikawa, K., Falkner, A.L., and Lin, D. (2017). Ventromedial Hypothalamus and the Generation of Aggression. Front. Syst. Neurosci. *11*, 94. https://doi.org/10.3389/fnsys.2017.00094.
55. Froemke, R.C., and Young, L.J. (2021). Oxytocin, Neural Plasticity, and Social Behavior. Annu. Rev. Neurosci. *44*, 359–381. https://doi.org/10.1146/annurev-neuro-102320-102847.
56. de Jong, T.R., and Neumann, I.D. (2018). Oxytocin and Aggression. Curr. Top. Behav. Neurosci. *35*, 175–192. https://doi.org/10.1007/7854_2017_13.
57. Berendzen, K.M., Sharma, R., Mandujano, M.A., Wei, Y., Rogers, F.D., Simmons, T.C., Seelke, A.M.H., Bond, J.M., Larios, R., Goodwin, N.L., et al. (2023). Oxytocin receptor is not required for social attachment in prairie voles. Neuron *111*, 787–796.e4. https://doi.org/10.1016/j.neuron.2022.12.011.
58. Anpilov, S., Shemesh, Y., Eren, N., Harony-Nicolas, H., Benjamin, A., Dine, J., Oliveira, V.E.M., Forkosh, O., Karamihalev, S., Hüttl, R.-E., et al. (2020). Wireless Optogenetic Stimulation of Oxytocin Neurons in a Semi-natural Setup Dynamically Elevates Both Pro-social and Agonistic Behaviors. Neuron *107*, 644–655.e7. https://doi.org/10.1016/j.neuron.2020.05.028.
59. Bale, T.L., Dorsa, D.M., and Johnston, C.A. (1995). Oxytocin receptor mRNA expression in the ventromedial hypothalamus during the estrous cycle. J. Neurosci. *15*, 5058–5064. https://doi.org/10.1523/JNEUROSCI.15-07-05058.1995.
60. Dumais, K.M., and Veenema, A.H. (2016). Vasopressin and oxytocin receptor systems in the brain: Sex differences and sex-specific regulation of social behavior. Front. Neuroendocrinol. *40*, 1–23. https://doi.org/10.1016/j.yfrne.2015.04.003.
61. Delville, Y., Mansour, K.M., and Ferris, C.F. (1996). Testosterone facilitates aggression by modulating vasopressin receptors in the hypothalamus. Physiol. Behav. *60*, 25–29. https://doi.org/10.1016/0031-9384(95)02246-5.
62. Lischinsky, J.E., and Lin, D. (2020). Neural mechanisms of aggression across species. Nat. Neurosci. *23*, 1317–1328. https://doi.org/10.1038/s41593-020-00715-2.
63. Anderson, D.J. (2016). Circuit modules linking internal states and social behaviour in flies and mice. Nat. Rev. Neurosci. *17*, 692–704. https://doi.org/10.1038/nrn.2016.125.
64. Lee, H., Kim, D.W., Remedios, R., Anthony, T.E., Chang, A., Madisen, L., Zeng, H., and Anderson, D.J. (2014). Scalable control of mounting and attack by Esr1+ neurons in the ventromedial hypothalamus. Nature *509*, 627–632. https://doi.org/10.1038/nature13169.
65. Vinograd, A., Nair, A., Kim, J., Linderman, S.W., and Anderson, D.J. (2024). Causal evidence of a line attractor encoding an affective state. Nature. https://doi.org/10.1038/s41586-024-07915-x.
66. Remedios, R., Kennedy, A., Zelikowsky, M., Grewe, B.F., Schnitzer, M.J., and Anderson, D.J. (2017). Social behaviour shapes hypothalamic neural ensemble representations of conspecific sex. Nature *550*, 388–392. https://doi.org/10.1038/nature23885.
67. Knoedler, J.R., Inoue, S., Bayless, D.W., Yang, T., Tantry, A., Davis, C.H., Leung, N.Y., Parthasarathy, S., Wang, G., Alvarado, M., et al. (2022). A functional cellular framework for sex and estrous cycle-dependent gene expression and behavior. Cell *185*, 654–671.e622. https://doi.org/10.1016/j.cell.2021.12.031.
68. Kim, D.-W., Yao, Z., Graybuck, L.T., Kim, T.K., Nguyen, T.N., Smith, K.A., Fong, O., Yi, L., Koulena, N., Pierson, N., et al. (2019). Multimodal analysis of cell types in a hypothalamic node controlling social behavior. Cell *179*, 713–728.e17. https://doi.org/10.1016/j.cell.2019.09.020.
69. Osakada, T., Yan, R., Jiang, Y., Wei, D., Tabuchi, R., Dai, B., Wang, X., Zhao, G., Wang, C.X., Liu, J.J., et al. (2024). A dedicated hypothalamic oxytocin circuit controls aversive social learning. Nature *626*, 347–356. https://doi.org/10.1038/s41586-023-06958-w.
70. Karigo, T., Kennedy, A., Yang, B., Liu, M., Tai, D., Wahle, I.A., and Anderson, D.J. (2021). Distinct hypothalamic control of same- and opposite-sex mounting behaviour in mice. Nature *589*, 258–263. https://doi.org/10.1038/s41586-020-2995-0.
71. Yang, C.F., Chiang, M.C., Gray, D.C., Prabhakaran, M., Alvarado, M., Juntti, S.A., Unger, E.K., Wells, J.A., and Shah, N.M. (2013). Sexually dimorphic neurons in the ventromedial hypothalamus govern mating in both sexes and aggression in males. Cell *153*, 896–909. https://doi.org/10.1016/j.cell.2013.04.017.
72. Dana, H., Sun, Y., Mohar, B., Hulse, B.K., Kerlin, A.M., Hasseman, J.P., Tsegaye, G., Tsang, A., Wong, A., Patel, R., et al. (2019). High-performance calcium sensors for imaging activity in neuronal populations and microcompartments. Nat Methods *16*, 649–657. https://doi.org/10.1038/s41592-019-0435-6.
73. Ragnauth, A.K., Goodwillie, A., Brewer, C., Muglia, L.J., Pfaff, D.W., and Kow, L.M. (2004). Vasopressin stimulates ventromedial hypothalamic neurons via oxytocin receptors in oxytocin gene knockout male and female mice. Neuroendocrinology *80*, 92–99. https://doi.org/10.1159/000081844.
74. Inenaga, K., Karman, H., Yamashita, H., Tribollet, E., Raggenbass, M., and Dreifuss, J.J. (1991). Oxytocin excites neurons located in the ventromedial nucleus of the Guinea-pig hypothalamus. J. Neuroendocrinol. *3*, 569–573. https://doi.org/10.1111/j.1365-2826.1991.tb00318.x.
75. Song, Z., and Albers, H.E. (2018). Cross-talk among oxytocin and arginine-vasopressin receptors: Relevance for basic and clinical studies of the brain and periphery. Front. Neuroendocrinol. *51*, 14–24. https://doi.org/10.1016/j.yfrne.2017.10.004.
76. Kabadi, A.M., Ousterout, D.G., Hilton, I.B., and Gersbach, C.A. (2014). Multiplex CRISPR/Cas9-based genome engineering from a single lentiviral vector. Nucleic Acids Res. *42*, e147. https://doi.org/10.1093/nar/gku749.
77. Sarin, S., Zuniga-Sanchez, E., Kurmangaliyev, Y.Z., Cousins, H., Patel, M., Hernandez, J., Zhang, K.X., Samuel, M.A., Morey, M., Sanes, J.R., and Zipursky, S.L. (2018). Role for Wnt Signaling in Retinal Neuropil Development: Analysis via RNA-Seq and In Vivo Somatic CRISPR Mutagenesis. Neuron *98*, 109–126.e8. https://doi.org/10.1016/j.neuron.2018.03.004.

78. Sentmanat, M.F., Peters, S.T., Florian, C.P., Connelly, J.P., and Pruett-Miller, S.M. (2018). A Survey of Validation Strategies for CRISPR-Cas9 Editing. Sci. Rep. *8*, 888. https://doi.org/10.1038/s41598-018-19441-8.

79. Brinkman, E.K., Chen, T., Amendola, M., and van Steensel, B. (2014). Easy quantitative assessment of genome editing by sequence trace decomposition. Nucleic Acids Res. *42*, e168. https://doi.org/10.1093/nar/gku936.

80. Egashira, N., Tanoue, A., Matsuda, T., Koushi, E., Harada, S., Takano, Y., Tsujimoto, G., Mishima, K., Iwasaki, K., and Fujiwara, M. (2007). Impaired social interaction and reduced anxiety-related behavior in vasopressin V1a receptor knockout mice. Behav. Brain Res. *178*, 123–127. https://doi.org/10.1016/j.bbr.2006.12.009.

81. Wersinger, S.R., Caldwell, H.K., Martinez, L., Gold, P., Hu, S.B., and Young, W.S., 3rd. (2007). Vasopressin 1a receptor knockout mice have a subtle olfactory deficit but normal aggression. Genes Brain Behav. *6*, 540–551. https://doi.org/10.1111/j.1601-183X.2006.00281.x.

82. Ferris, C.F. (2005). Vasopressin/oxytocin and aggression. Novartis Found. Symp. *268*, 190–200. https://doi.org/10.1002/0470010703.ch13.

83. DeVries, A.C., Young, W.S., 3rd, and Nelson, R.J. (1997). Reduced aggressive behaviour in mice with targeted disruption of the oxytocin gene. J. Neuroendocrinol. *9*, 363–368. https://doi.org/10.1046/j.1365-2826.1997.t01-1-00589.x.

84. Ghosh, K.K., Burns, L.D., Cocker, E.D., Nimmerjahn, A., Ziv, Y., Gamal, A.E., and Schnitzer, M.J. (2011). Miniaturized integration of a fluorescence microscope. Nat. Methods *8*, 871–878. https://doi.org/10.1038/nmeth.1694.

85. Tuladhar, R., Yeu, Y., Tyler Piazza, J., Tan, Z., Rene Clemenceau, J., Wu, X., Barrett, Q., Herbert, J., Mathews, D.H., Kim, J., et al. (2019). CRISPR-Cas9-based mutagenesis frequently provokes on-target mRNA misregulation. Nat. Commun. *10*, 4056. https://doi.org/10.1038/s41467-019-12028-5.

86. Yang, B., Karigo, T., and Anderson, D.J. (2022). Transformations of neural representations in a social behaviour network. Nature *608*, 741–749. https://doi.org/10.1038/s41586-022-05057-6.

87. Zhang, Y., Rozsa, M., Liang, Y., Bushey, D., Wei, Z., Zheng, J., Reep, D., Broussard, G.J., Tsang, A., Tsegaye, G., et al. (2023). Fast and sensitive GCaMP calcium indicators for imaging neural populations. Nature *615*, 884–891. https://doi.org/10.1038/s41586-023-05828-9.

88. Lerner, T.N., Shilyansky, C., Davidson, T.J., Evans, K.E., Beier, K.T., Zalocusky, K.A., Crow, A.K., Malenka, R.C., Luo, L., Tomer, R., and Deisseroth, K. (2015). Intact-Brain Analyses Reveal Distinct Information Carried by SNc Dopamine Subcircuits. Cell *162*, 635–647. https://doi.org/10.1016/j.cell.2015.07.014.

89. Egorov, A.V., Hamam, B.N., Fransén, E., Hasselmo, M.E., and Alonso, A.A. (2002). Graded persistent activity in entorhinal cortex neurons. Nature *420*, 173–178. https://doi.org/10.1038/nature01171.

90. Heys, J.G., Schultheiss, N.W., Shay, C.F., Tsuno, Y., and Hasselmo, M.E. (2012). Effects of acetylcholine on neuronal properties in entorhinal cortex. Front. Behav. Neurosci. *6*, 32. https://doi.org/10.3389/fnbeh.2012.00032.

91. Liu, J.J., Eyring, K.W., König, G.M., Kostenis, E., and Tsien, R.W. (2022). Oxytocin-Modulated Ion Channel Ensemble Controls Depolarization, Integration and Burst Firing in CA2 Pyramidal Neurons. J. Neurosci. *42*, 7707–7720. https://doi.org/10.1523/JNEUROSCI.0921-22.2022.

92. Cavanagh, S.E., Towers, J.P., Wallis, J.D., Hunt, L.T., and Kennerley, S.W. (2018). Reconciling persistent and dynamic hypotheses of working memory coding in prefrontal cortex. Nat. Commun. *9*, 3498. https://doi.org/10.1038/s41467-018-05873-3.

93. Murray, J.D., Bernacchia, A., Freedman, D.J., Romo, R., Wallis, J.D., Cai, X., Padoa-Schioppa, C., Pasternak, T., Seo, H., Lee, D., and Wang, X.J. (2014). A hierarchy of intrinsic timescales across primate cortex. Nat. Neurosci. *17*, 1661–1663. https://doi.org/10.1038/nn.3862.

94. Shao, Y.Q., Fan, L., Wu, W.Y., Zhu, Y.J., and Xu, H.T. (2022). A developmental switch between electrical and neuropeptide communication in the ventromedial hypothalamus. Curr. Biol. *32*, 3137–3145.e3. https://doi.org/10.1016/j.cub.2022.05.029.

95. Stagkourakis, S., Spigolon, G., Liu, G., and Anderson, D.J. (2020). Experience-dependent plasticity in an innate social behavior is mediated by hypothalamic LTP. Proc. Natl. Acad. Sci. USA *117*, 25789–25799. https://doi.org/10.1073/pnas.2011782117.

96. Koulakov, A.A., Raghavachari, S., Kepecs, A., and Lisman, J.E. (2002). Model for a robust neural integrator. Nat. Neurosci. *5*, 775–782. https://doi.org/10.1038/nn893.

97. Goldman, M.S., Levine, J.H., Major, G., Tank, D.W., and Seung, H.S. (2003). Robust persistent neural activity in a model integrator with multiple hysteretic dendrites per neuron. Cereb. Cortex *13*, 1185–1195. https://doi.org/10.1093/cercor/bhg095.

98. Inagaki, H.K., Fontolan, L., Romani, S., and Svoboda, K. (2019). Discrete attractor dynamics underlies persistent activity in the frontal cortex. Nature *566*, 212–217. https://doi.org/10.1038/s41586-019-0919-7.

99. Simerly, R.B. (1990). Hormonal control of neuropeptide gene expression in sexually dimorphic olfactory pathways. Trends Neurosci. *13*, 104–110. https://doi.org/10.1016/0166-2236(90)90186-e.

100. McCulloch, K.A., Zhou, K., and Jin, Y. (2020). Neuronal transcriptome analyses reveal novel neuropeptide modulators of excitation and inhibition imbalance in C. elegans. PLoS One *15*, e0233991. https://doi.org/10.1371/journal.pone.0233991.

101. Inoue, S., Yang, R., Tantry, A., Davis, C.H., Yang, T., Knoedler, J.R., Wei, Y., Adams, E.L., Thombare, S., Golf, S.R., et al. (2019). Periodic Remodeling in a Neural Circuit Governs Timing of Female Sexual Behavior. Cell *179*, 1393–1408.e16. https://doi.org/10.1016/j.cell.2019.10.025.

102. Yin, L., Hashikawa, K., Hashikawa, Y., Osakada, T., Lischinsky, J.E., Diaz, V., and Lin, D. (2022). VMHvll(Cckar) cells dynamically control female sexual behaviors over the reproductive cycle. Neuron *110*, 3000–3017.e8. https://doi.org/10.1016/j.neuron.2022.06.026.

103. Teitler, M., and Herrick-Davis, K. (1994). Multiple serotonin receptor subtypes: molecular cloning and functional expression. Crit. Rev. Neurobiol. *8*, 175–188.

104. Zhou, P., Resendez, S.L., Rodriguez-Romaguera, J., Jimenez, J.C., Neufeld, S.Q., Giovannucci, A., Friedrich, J., Pnevmatikakis, E.A., Stuber, G.D., Hen, R., et al. (2018). Efficient and accurate extraction of in vivo calcium signals from microendoscopic video data. eLife *7*, e28728. https://doi.org/10.7554/eLife.28728.

105. Hong, W., Kennedy, A., Burgos-Artizzu, X.P., Zelikowsky, M., Navonne, S.G., Perona, P., and Anderson, D.J. (2015). Automated measurement of mouse social behaviors using depth sensing, video tracking, and machine learning. Proc. Natl. Acad. Sci. USA *112*, E5351–E5360. https://doi.org/10.1073/pnas.1515982112.

106. Segalin, C., Williams, J., Karigo, T., Hui, M., Zelikowsky, M., Sun, J.J., Perona, P., Anderson, D.J., and Kennedy, A. (2021). The Mouse Action Recognition System (MARS) software pipeline for automated analysis of social behaviors in mice. eLife *10*, e63720. https://doi.org/10.7554/eLife.63720.

107. Shadlen, M.N., Britten, K.H., Newsome, W.T., and Movshon, J.A. (1996). A computational analysis of the relationship between neuronal and behavioral responses to visual motion. J. Neurosci. *16*, 1486–1510. https://doi.org/10.1523/JNEUROSCI.16-04-01486.1996.

108. Maheswaranathan, N., Williams, A.H., Golub, M.D., Ganguli, S., and Sussillo, D. (2019). Reverse engineering recurrent networks for sentiment classification reveals line attractor dynamics. Adv. Neural Inf. Process. Syst. *32*, 15696–15705.

109. Li, Y., Mathis, A., Grewe, B.F., Osterhout, J.A., Ahanonu, B., Schnitzer, M.J., Murthy, V.N., and Dulac, C. (2017). Neuronal Representation of Social Information in the Medial Amygdala of Awake Behaving Mice. Cell *171*, 1176–1190.e17. https://doi.org/10.1016/j.cell.2017.10.015.

110. Hunker, A.C., Soden, M.E., Krayushkina, D., Heymann, G., Awatramani, R., and Zweifel, L.S. (2020). Conditional Single Vector CRISPR/SaCas9 Viruses for Efficient Mutagenesis in the Adult Mouse Nervous System. Cell Rep. *30*, 4303–4316.e6. https://doi.org/10.1016/j.celrep.2020.02.092.

111. Melzer, S., Newmark, E.R., Mizuno, G.O., Hyun, M., Philson, A.C., Quiroli, E., Righetti, B., Gregory, M.R., Huang, K.W., Levasseur, J., et al. (2021). Bombesin-like peptide recruits disinhibitory cortical circuits and enhances fear memories. Cell *184*, 5622–5634.e25. https://doi.org/10.1016/j.cell.2021.09.013.

112. Castro, D.C., Oswell, C.S., Zhang, E.T., Pedersen, C.E., Piantadosi, S.C., Rossi, M.A., Hunker, A.C., Guglin, A., Morón, J.A., Zweifel, L.S., et al. (2021). An endogenous opioid circuit determines state-dependent reward consumption. Nature *598*, 646–651. https://doi.org/10.1038/s41586-021-04013-0.

113. Soden, M.E., Yee, J.X., and Zweifel, L.S. (2023). Circuit coordination of opposing neuropeptide and neurotransmitter signals. Nature *619*, 332–337. https://doi.org/10.1038/s41586-023-06246-7.

114. Swiech, L., Heidenreich, M., Banerjee, A., Habib, N., Li, Y., Trombetta, J., Sur, M., and Zhang, F. (2015). In vivo interrogation of gene function in the mammalian brain using CRISPR-Cas9. Nat. Biotechnol. *33*, 102–106. https://doi.org/10.1038/nbt.3055.

STAR★METHODS

KEY RESOURCES TABLE

REAGENT or RESOURCE	SOURCE	IDENTIFIER
Antibodies		
DsRed	Living Colors	#632496
Cas9	Novus Biologicals	#NBP2-36440
Cas9	Cell Signaling	#14697
HA-epitope	Cell Signaling	#3724
HA-epitope	Santa Cruz	# f7 sc-7392
Myc-epitope	Cell Signaling	#2276
Myc-epitope	Cell Signaling	#2278
Bacterial and virus strains		
LV-CMV-SpCas9	signagen	#SL100310
pLV $gRNA_{scramble}$ ubc-DsRed	Janelia viral core	N/A
pLV $gRNA_{Oxtr/Avpr1a}$ ubc-DsRed	Janelia viral core	N/A
AAV1-Syn-Flex-GCaMP7f	addgene	#104492
AAVDJ/8-EFS-NC-SpCas9-HA -NLS-Poly(A)	Duke viral cores	N/A
AAV9-EFS-NC-SpCas9-HA -NLS-Poly(A)	Janelia; Duke viral cores	N/A
AAV9-hPGK-NC-SpCas9-HA -NLS-Poly(A)	Janelia; Duke viral cores	N/A
AAV9-EFS-SpCas9-myc	Janelia	N/A
AAV9-CMV-NC-SpCas9-HA -NLS-Poly(A)	Duke viral cores	N/A
AAV9-EFS-NC-DIO-SpCas9-myc-NLS-Poly(A)	Janelia; Duke viral cores	N/A
AAV9-hPGK-DIO-SpCas9-myc-NLS-Poly(A)	Janelia; Duke viral cores	N/A
AAV1-$gRNAs_{scramble}$-hSyn flex-GCaMP8s	Janelia	N/A
AAV1-$gRNAs_{Oxtr/1Avpr1a}$-hSyn flex-GCaMP8s	Janelia	N/A
One Shot™ Stbl3™	Thermo Fisher Scientific	#C737303
Sure2	Agilent	#200152
Chemicals, peptides, and recombinant proteins		
Oxytocin	Tocris	#1910
Vasopressin	Tocris	#2935
T7 endonuclease	NEB	#M0302
CNQX disodium salt	Tocris	#1045
(+)-MK 801 maleate	Tocris	#092410
Deposited data		
Neuronal recordings from $VMHvl^{Esr1}$ neurons in experimental and control groups	This paper	DANDI repository: DANDI:001131
Experimental models: Cell lines		
Cell line: Neuro2a	ATCC	CCL-131
Cell line: Neuro2a-Cas9	This paper	N/A
Experimental models: Organisms/strains		
Mouse: Esr1-Cre	Lee et al.[64]	N/A
Mouse: C57BL/6N	Charles River	N/A
Mouse: BALB/c	Charles River	N/A
Oligonucleotides		
$SgRNA_{scramble}$ GCGCCAAACGTGCCCTGACG	This paper	N/A

(*Continued on next page*)

Continued

REAGENT or RESOURCE	SOURCE	IDENTIFIER
$SgRNA_{AVPR1a-1}$ GCCGGGGGACGTACGCAACG	This paper	N/A
$SgRNA_{AVPR1a-2}$ CGGGCAACTCCAGCCCGTGG	This paper	N/A
$SgRNA_{OXTR-1}$ ACGTCGCCAGCACCGCCAGG	This paper	N/A
$SgRNA_{OXTR-2}$ GGACGGCGTCTTCGATTGCT	This paper	N/A
Recombinant DNA		
EFS-SpCas9-Blast	addgene	#52962
ph7SK-gRNA	addgene	#53189
phH1-gRNA	addgene	#53186
pmU6-gRNA	addgene	#53187
phU6-gRNA	addgene	#53188
GG hUbC-dsRED	addgene	#84034
hSyn-FLEX-jGCaMP8s-WPRE	addgene	#162377
pX551-CMV-SpCas9	addgene	#107024
EFS-SpCas9	addgene	#104588
pGP-AAV-syn-FLEX-jGCaMP7f-WPRE	addgene	#104492
hSyn-FLEX-jGCaMP8s-WPRE	addgene	#162377
$gRNA_{scramble}$-hSyn flex-GCaMP8s	This paper	N/A
$gRNAs_{Oxtr/1Avpr1a}$ -hSyn flex- GCaMP8s	This paper	N/A
EFS-NC-SpCas9-NLS-Poly(A)	DUKE	#pBK694
hPGK-DIO-SpCas9-myc-NLS-Poly(A)	This paper	N/A
EFS-NC-DIO-SpCas9-myc-NLS-Poly(A)	This paper	N/A
Software and algorithms		
Matlab	MathWorks	https://www.mathworks.com
Prism	GraphPad Software	https://www.graphpad.com/
ImageJ	NIH	https://imagej.nih.gov/ij
Snapgene	Snapgene	https://www.snapgene.com
Tracking of INDELs by Decomposition (TIDE)	Brinkman et al.[79]	http://tide.nki.nl
VivoViewer (Matlab)	This paper	N/A
StreamPix	Norpix	https://www.norpix.com/products/streampix/streampix.php
Inscopix Data Acquisition Software	Inscopix	https://inscopix.com/
CNMF-E (Matlab)	Zhou et al., 2018[104]	https://github.com/zhoupc/CNMF_E
rSLDS (Dynamical system modelling in Python)	Nair et al., 2023[21]	https://github.com/lindermanlab/ssm
Additional code for flowfield and 3D landscape vidualization	Nair et al., 2023[21]	https://github.com/DJALab/VMHvl_MPOA_dynamics

RESOURCE AVAILABILITY

Lead contact

Requests for resources and reagents should be addressed to lead contact, David J. Anderson (wuwei@caltech.edu).

Materials availability

Materials generated in this study will be made available upon reasonable request.

Data and code availability

- The source data used in this paper will be deposited in DANDI: #001131 and can be shared by the lead contact upon reasonable request.

- Code used for analyses in this paper is publicly available in the following repositories: https://github.com/lindermanlab/ssm and https://github.com/DJALab/VMHvl_MPOA_dynamics.
- Any additional information required to reanalyze the data reported in the paper is available from the lead contact upon reasonable request.

EXPERIMENTAL MODEL AND STUDY PARTICIPANT DETAILS

All procedures were performed in accordance with NIH guidelines and approved by the Institutional Animal Care and Use Committee (IACUC) at the California Institute of Technology (Caltech). We used 8-10 weeks *Esr1*$^{Cre/+}$[64] transgenic mice. Animals were housed and maintained on a reverse 12 h light-dark cycle with food and water ad libitum. We used 8-10 weeks wild-type (WT) C57BL/6N male mice (experimental), 8-10 weeks C57BL/6N female mice or BALB/c females (for sexual experience), and 8-10 weeks BALB/c male mice (intruders) were obtained from Charles River (Burlington, MA). Behavior was tested during the dark cycle.

Viruses

The following AAVs were used in this study, with injection titers as indicated. Viruses with a high original titer were diluted with clean PBS on the day of use. AAV1-Syn-Flex-GCaMP7f (2.1 x e^{13}) was purchased from Addgene. AAVDJ/8-EFS-NC-SpCas9-HA -NLS-Poly(A) (pBK694) (2.00x e^{13}) and AAV9-EFS-NC-SpCas9-HA -NLS-Poly(A) (2.17x e^{13}) purchased from Duke viral vector core. The AAV9-EFS-NC-DIO-SpCas9-myc-NLS-Poly(A) (2.31x+e^{13}), AAV9-hPGK-DIO-SpCas9-myc-NLS-Poly(A) (2.31x+e^{13}), pAAV-CMV-SpCas9-NLS-Poly(A) (7x+e^{12}), AAV1-gRNAs$_{scramble}$-hSyn flex-GCaMP8s-wpre (2.75x e^{12}) and AAV1-gRNAs$_{Oxtr/1Avpr1a}$ -hSyn flex-GCaMP8s-wpre (2.44x e^{12}) were packaged at the HHMI Janelia Research Campus virus and the Duke Viral core facilities. Viruses with hPGK or Efs promoters were used interchangeably to drive the expression of Cas9. In the illustration in Figures 2Aii and 3Aii only the Efs promoter is depicted for simplicity reasons. The RNAs$_{scramble}$-ubc DsRed (TU/ML 1.5X e^{8}) and RNAs$_{Oxtr/Avpr1a}$ ubc DsRed (OXTR/AVPR1a) lentiviruses (TU/ML 3.50 X e^{8}) were also packaged at the HHMI Janelia Research Campus virus facility.

METHOD DETAILS

Generation of multiplex CRISPR/*Streptococcus pyogenes* Cas9 vectors

The multiplex gRNAs construct was based on the backbone of pLV GG hUbC-dsRED (addgene #84034) after being modified to remove superfluous sequences (e.g., LoxP). Individual gRNAs were cloned as described in Kabadi et al.[76] Cas9 pAAV-EFS-NC-SpCas9-NLS-Poly(A) (Duke viral vector core) vectors were used for constitutive Cas9 expression. For Cre-dependent CRISPR/Cas9 DIO/FLEX, sequences were cloned in pAAV-EFS-NC-SpCas9-NLS-Poly(A) vectors, respectively. The Golden Gate cassette to express four gRNAs was cloned into the pGP-AAV-syn-FLEX-jGCaMP8s-WPRE (addgene 162377)[87] vector. Four different gRNAs are constitutively being expressed under four different polymerase III promoters, and a Cre-dependent expression of the calcium indicator jGCaMP8s under the express human synapsing promoter.

Generation of Neuro2A constitutively expressed CAS9 cells and screening of gRNAs

Neuro2a cells (ATCC CCL-131™) were transfected with EFS-Cas9-Blast plasmid (addgene # 52962) and selected for four days with blasticidin antibiotic. Individual gRNAs were cloned in ph7SK-gRNA (addgene # 53189) or phH1-gRNA (addgene # 53186) or pmU6-gRNA (addgene # 53187) or phU6-gRNA (addgene # 53188) plasmids, 0.5-1 ug transfected in Neuro2a-Cas9 cells and after three days genomic DNA was isolated. We used T7 endonuclease assay for testing the efficiency of each gRNAs to generate edits, similar to what has been described in https://www.neb.com/protocols/2014/08/11/determining-genome-targeting-efficiency-using-t7-endonuclease-i. In addition, Sanger traces were generated with target-specific PCR and analyzed with the Tracking of INDELs by Decomposition (TIDE) web tool http://tide.nki.nl (data not shown).

Screening for aggressor male and resident intruder assay

All experimental male mice (''residents'') were individually housed for two weeks and received sexual experience (for at least one week). Previously it has been reported that ~20-25% of inbreeding C57BL/6N male animals fail to display territorial aggression against conspecific male intruders during the RI assay.[95] We pre-screened males for baseline aggression using resident-intruder testing sessions to identify and exclude no aggressors from our analysis. Animals that attacked two constitutively presented intruders were termed aggressors and added to the pool of animals for CRISRP/Cas9-based gene editing surgeries. On the experimental day, the preselected male residents were transported in their home cage to a novel behavioral testing room (under infrared light), where they acclimated for 5-10 min. An unfamiliar group housed BALB/c mouse (''intruder'') was then placed in the resident's home cage, and residents were allowed to interact with it for period of time.

Acute brain slices preparation

Briefly, male adult mice were anesthetized with isoflurane and transcardially perfused with cold NMDG-ACSF (adjusted to pH 7.3–7.4) containing CaCl2 (0.5 mM), glucose (25 mM), HCl (92 mM), HEPES (20 mM), KCl (2.5 mM), kynurenic acid (1 mM), MgSO4

(10 mM), NaHCO3 (30 mM), NaH2PO4 (1.2 mM), NMDG (92 mM), sodium L-ascorbate (5 mM), sodium pyruvate (3 mM), thiourea (2 mM), bubbled with carbogen gas (95% O_2 and 5% CO_2). The brain was sectioned at 250 μm using a vibratome (VT1000S, Leica Microsystems) on ice and was incubated in 34oc for 12 min, in NMDG – ACSF. Then transfer the sections to room temperature in aCSF/HEPES-GSH solution (adjusted to pH 7.3–7.4,) containing CaCl2(2 mM), glucose (25 mM), kCl (2.5 mM), HEPES (20 mM), NaCl (92 mM), MgSO4 (2 mM), NaHCO3 (30 mM), NaH2PO4 (1.2 mM), sodium L-ascorbate (5 mM), sodium pyruvate (3 mM), thiourea (2 mM), and Glutathione Monoethyl Ester (0.5-1mM)-before proceeding with Ca^{2+} imaging.

Peptide perfusion and two-photon calcium imaging experiments

Solutions of 400nM of Oxt and/or Avp, 20 μM CNQX and 10 peptides μM (Tocris) were prepared in aCSF and perfused with a rate of 1-2ml/min through a microfluidics chamber containing the brain slices. Calcium imaging was performed using a custom-modified Ultima two-photon laser scanning microscope (Bruker). The primary beam path was equipped with galvanometers driving a Chameleon Ultra II Ti:Sapphire laser (Coherent) and used for GCaMP imaging (920 nm). GCaMP emission was detected with photomultiplier-tube (Hamamatsu). Images were acquired with an Olympus20X XLUMPLFLN Objective, 1.00 NA, 2.0 mm WD. All image acquisition was performed using PrairieView Software (Version 5.3) with a framerate of ∼1.2Hz.

Behavior recording

All behavioral experiments were performed in conventional mouse housing cages (home cage or new cage) under red lighting, using the previously described behavior recording setup.[105] The behavior video's top and front views were acquired at 30 Hz using the video recording software, StreamPix7 (Norpix).

Behavior annotations

Behavior videos were processed using an automated behavior classification system to generate frame-by-frame annotations of attack, mounting and sniffing behavior.[106] The output of the classifier and behavior videos were loaded into a MATLAB based MATLAB-based behavior annotation interface and then manually corrected by trained individuals to produce a final set of annotations.[106] A 'baseline' period of 5-minutes was recorded at the start of every recording session during which the animal was alone in its home cage. Six behaviors were annotated during the resident intruder assays: sniff (face, body, genital-directed sniffing), towards male or female intruders, and attack-, mount- directed behavior against male or female intruders. Post-surgery, male residents were exposed to a male intruder first, and subsequently to a female intruder. RI assay with a male or a female intruder was performed on separate days, except during CRISPRoscopy. For quantifying the interval (s) between behavioral bouts in Figures 2, 3, S2, and S3, animals that show ≤1 mount or attack bout were excluded. 15 min for male-male interaction was scored in Figures 2 and S2. In Figures 3 and S3 ∼15-20 min of RI was scored for male -male interaction. 10 min of male-female interaction was scored during the RI assays in Figures 2, 3, S2 and S3.

In addition to the classification of behaviors, automated pose estimation was performed on behavior videos to obtain key points of interacting mice.[106] The velocity of the resident mouse was calculated as the change in positions of centroids of the head and hips, computed across two consecutive frames as previously performed.[70] The distribution of this feature was computed for both experimental and control animals to obtain the data shown in Figure S2Ciii.

Stereotaxic surgery

Surgeries were performed on socially and sexually experienced adult male *Esr1*$^{Cre/+}$ mice mice 8–12 weeks old. Virus injection and implantation were performed as described previously.[66,70] Briefly, animals were anesthetized with isoflurane (5% for induction and 1.5% for maintenance) and placed on a stereotaxic frame (David Kopf Instruments). The virus was injected into the target area using a pulled-glass capillary (World Precision Instruments) and a pressure injector (Micro4 controller, World Precision Instruments) at a 20 nl /min flow rate. The glass capillary was left in place for 5 -10 minutes following injection before withdrawal. The injection viral volumes were ∼400-500nl for bilateral injection in mice used for behavioral analysis and fiberphotometry. For micro endoscope recordings, we performed unilateral ∼200nl viral injections. The Stereotaxic injection coordinates were based on the Paxinos and Franklin atlas (posterior VMHvl, anterior–posterior: −4.68, medial–lateral: ±0.73, dorsal–ventral: −5.73). For single fiber optogenetic and fiber photometry experiments (optogenetics: diameter 200 μm, N.A., 0.22; fiber photometry: diameter 400 μm, N.A., 0.48; Doric lenses) were then placed above the virus injection sites (fiber photometry: 150 μm above) and fixed on the skull with dental cement (Metabond, Parkell). For micro-endoscope experiments, virus injection and lens implantation were performed on the same day Lenses with a baseplate were slowly lowered into the brain and fixed to the skull with dental cement. Mice were habituated with weight-matched dummy micro-endoscopes (Inscopix) for at least one week before behavior testing. Mice were head-fixed on a running wheel 3-4 weeks after lens implantation, and a miniaturized micro-endoscope (nVista, Inscopix) was attached to the baseplate for imaging. Mice were singly housed after surgery and were allowed to recover for at least 4 weeks before behavioral testing.

Histology

Once the behavioral experiments were finished, virus expression and implant placement were histologically verified on all mice. Mice lacking correct virus expression or implant placement were excluded from the analysis. Mice were transcardially perfused with 1x PBS at room temperature, followed by 4% paraformaldehyde (PFA) (diluted from 16% EM grade PFA). Brains were extracted and

post-fixed in 4% PFA 16-24h at 4°C, followed by 24 hours in 30% sucrose/PBS at 4°C. Brains were embedded in OCT mounting medium, frozen on dry ice and stored at −80°C for subsequent sectioning. Brains were sectioned into 60 μm slices on a cryostat (Leica Biosystems). Sections were washed with 1× PBS and mounted on Superfrost slides, then incubated for 15 minutes at room temperature in DAPI/PBS (0.5 μg/ml) for counterstaining, rewashed and coverslipped. Sections were imaged with an epifluorescent microscope (Olympus VS120)

For some epitope staining 30 um sections were cut from either fresh-frozen tissue or post-fixed 2h 4%PFA on ice, immersed in 30% sucrose:1xPBS 4C 2h before embedding in OCT. For Cas9 immunostaining, a cocktail of antibodies against the Cas9-fused HA or Myc epitope and the Cas9 protein itself was used. Animals were stained after 9-12 weeks post-injection. Estimates of the co-indefectibility between the Cas9 and the gRNA expressing viruses were made at the center of the injection site

Fiberphotometry recordings

The fiber photometry setup was similar to what was previously described.[88] We used 470 nm LEDs (M470F3, Thorlabs, filtered with 470-10 nm bandpass filters FB470-10, Thorlabs) for fluorophore excitation and 405 nm LEDs for isosbestic excitation (M405FP1, Thorlabs, filtered with 410–10 nm bandpass filters FB410-10, Thorlabs). LEDs were modulated at 208 Hz (470 nm) and 333 Hz (405 nm) and controlled by a real-time processor (RZ5P, Tucker David Technologies) via an LED driver (DC4104, Thorlabs). The emission signal from the 470 nm excitation was normalized to the emission signal from the isosbestic excitation (405 nm), to control for motion artifacts, photobleaching, and levels of GCaMP8s expression. LEDs were coupled to a 425 nm longpass dichroic mirror (Thorlabs, DMLP425R) via fiber optic patch cables (diameter 400 μm, N.A., 0.48; Doric lenses). Emitted light was collected via the patch cable, coupled to a 490 nm long pass dichroic mirror (DMLP490R, Thorlabs), filtered (FF01-542/27-25, Sem- rock), collimated through a focusing lens (F671SMA-405, Thorlabs) and detected by the photodetectors (Model 2151, Newport). Recordings were acquired using Synapse software (Tucker Davis Technologies). On the test day, after at least 5 minutes of acclimation under the recording setup, the male resident was first recorded for 1 minute to establish a baseline. Male or female intruders were introduced into the home cage on separate days. Typically, each session lasted 15-20 min.

Microendoscope recordings

On the day of imaging, mice were habituated for at least 5-10 minutes after installing the micro endoscope in their home cage before the start of the behavior tests. Imaging data were acquired at 30 Hz with 2× spatial down sampling; light-emitting diode power (0.1–0.5) and gain (1–7×) were adjusted depending on the brightness of GCaMP expression as determined by the image histogram according to the user manual. A transistor–transistor logic (TTL) pulse from the Sync port of the data acquisition box (DAQ, Inscopix) was used for synchronous triggering of StreamPix7 (Norpix) for video recording. Imaging sessions typically lasted 1 h (20–25 min interactions per sex).

Microendoscope data extraction

Preprocessing and Calcium data extraction was performed similarly to what has been previously described.[86] Briefly, data were 2x downsampled, motion corrected, and a spatial band-pass filter was applied to remove the out-of-focus background. Next, filtered imaging data were temporally downsampled to 10 Hz. Calcium traces were extracted and deconvolved using the CNMF-E[104] with the following parameters: patch_dims = [42, 42], gSig = 3, gSiz = 13, ring_radius = 19, min_corr ∼0.57-0.62, min_pnr = ∼5.5-6, deconvolution: foopsi with the ar1 model. Every extracted unit's spatial and temporal components were manually inspected (SNR, PNR, size, motion artifacts, decay kinetics, etc.). Traces of units were either z-scored or normalized in units of σ relative to the baseline fluorescence (during 7sec or more) of the neuron before the first trial of resident-intruder interactions, as previously described,[70,86] Distinct hypothalamic control of same-and opposite-sex mounting behavior in mice. In Figure S5C, the z-scored value during a behavioral bout for each unit was normalized by subtracting the mean of a 2-3 sec baseline before the onset of the bout. The average normalized activity was quantified for a period of 15 sec. A total of 585 units (n=5 mice) from control and 546 units (n=7 mice) from experimental mice were recorded.

QUANTIFICATION AND STATISTICAL ANALYSIS

Transcriptomic analysis of *Esr1*, *Oxtr*, *Avpr1a* mRNAs

The violin plots, t-SNE and the quantification of *Esr1*, *Oxtr*, *Avpr1a* mRNAs in the different single cell VMH clusters (Figures 1B, S1B, and S1D) or in single Esr1+ cells (Figure 1D) were analyzed as described previously.[68]

Fiberphotometry analysis

All data analyses were performed in Matlab 2020a and Python 3.8.3 as previously described.[70,86] Briefly, behavioral video files and fiber photometry data were obtained in a time-locked manner. Photometry recordings yielded both a 405-nm (isosbestic, Ca^{2+} independent) signal and a 470-nm (Ca^{2+} dependent)) signal. To align the 405-nm signal to the 470-nm signal, a least squares linear fit is first performed. The motion corrected 470-nm signal is obtained as follows: $[F_{470}(t) - F_{405}(t)] / F_{405}(t)$. To normalize activity, the baseline value F_0 and standard deviation SD_0. were calculated using a 2 second window as follows $[F_n(t) - F_0(t)] / SD_0$. Overlapping behavioral bouts within this time window were excluded from the analysis. The peak and area under the normalized activity

curve (AUC) were calculated within the 10-second window. We confirmed that the latency to achieve the peri-stimulus time histogram (PETH) peak level is shorter than the indicated time window. Quantifying neural activity during sniffing was performed over 1 minute of sniffing behavior following the introduction of the intruder.

Microendoscope neural data analysis

Choice probability

Choice probability (CP) analysis was used as before[70] to measure a cell's tuning, defined here as how well two conditions could be predictively discriminated from a single cell's activity.[107] The CP of a given cell for a pair of behavioral conditions was computed by constructing a histogram of that cell's $\Delta F(t)/F_0$ values under each of the two conditions. These two histograms were plotted against each other to generate a ROC (receiver-operating characteristic) curve. The integral of the area under this ROC curve generated the CP value for each cell with respect to each of the two behavioral conditions. This CP value is bounded from 0 to 1, where a CP of 0.5 indicates that the neuron's activity cannot distinguish between the two conditions. As in previous studies, the statistical significance of choice probabilities was determined relative to chance. We shuffled behavioral bout timings for each of the two compared conditions and computed the choice probability for this shuffled data. Shuffling was repeated 100 times for each of the two behaviors, from which we calculated the mean and s.d. (σ) of the 'shuffled' choice probabilities.

As significant, we considered any observed choice probabilities $>2\sigma$ above the shuffled mean and imposed an additional choice probability threshold > 0.7 as previously described.[70] The colored bars indicate the neurons that show a strong and statistically significant choice probability, and grey bars indicate cells for which the choice probability was either activated $< 2\ \sigma$ above (not responsive) the shuffled mean or was considered which choice probability not significantly higher than chance or choice probability ≤ 0.7 for that neuron.

Dimensionality reduction for visualizing intruder sex

Low-dimensional representations for visualizing changing ensemble dynamics over time were constructed using partial least squares (PLS) regression (MATLAB). For PLS, all traces were concatenated and regressed against a $1 \times T$ vector with entries valued at -1 (if a male intruder was present), 1 (if there was a female intruder), or 0 (otherwise).

Decoding intruder sex from neural data

We constructed a frame-wise linear SVM decoders (as described previously[66,70]) to distinguish intruder sex. Training data was constructed from the set of $N \times 1$ (N = neurons) population activity vectors from all frames occurring during social interaction in each mouse. Equal numbers of frames of male and female interaction were used during decoder training to ensure chance decoder performance of 50%. Shuffled decoder data were generated by the training the decoder on the same neural data but with behavior labels randomly assigned to each behavior bout (n=5 control and n=7 *expreimental mice*). This training data, along with intruder sex labels, was then used to train a linear SVM decoder. Accuracy was evaluated using a stratified fivefold cross-validator. Decoding was repeated 100 times, with decoder performance reported as the mean accuracy per imaged animal. For significance testing, the mean accuracy of the decoder trained on shuffled data (repeated 500 times per imaged animal) was computed to compare against the decoder accuracy trained on actual data.

Decoding behavior from neural activity

We constructed frame-wise linear SVM decoders (as described previously[66,70]) to discriminate male directed sniffing and attack from imaged control and experimental $VMHvl^{Esr1}$ units. Briefly manual annotations of sniffing behavior and attack behavior for each intruder male mouse were used to provide training labels of behavior type in control and experimental mice. Bar graphs of decoder accuracy (Figure S5E) were generated to discriminate sniffing and attack from imaged activity on individual frames of a behavior (sampled at 15 Hz). Equal numbers of sniff and attack frames (frame-wise decoder) were used during decoder training, to ensure chance decoder performance of 50%. 'Shuffled' decoder data were generated by training the decoder on the same neural data, but with sniff and attack behavior annotations randomly assigned to each behavior bout.

Decoding was repeated 20 times for each intruder and each imaged mouse, and decoder performance was reported as the average accuracy across imaged mice for control and experimental mice. For significance testing, the mean accuracy of the decoder trained on shuffled data was computed across mice, in each condition, and shuffling was repeated 1,000 times. Significance was determined across imaged mice using the Mann–Whitney U test between the mean accuracy of the decoders trained on real versus shuffled data.

Statistical analysis

Data were processed and analyzed using Python, MATLAB and GraphPad (GraphPad PRISM v.9). Data were analyzed using two-tailed, nested non-parametric tests. Wilcoxon signed-rank test (paired, non-parametric Mann–Whitney *U*-test) was used for binary paired samples. Kolmogorov–Smirnov test was used for non-paired samples plotted as ECDF graphs. N.s. $P > 0.05$, $^{*}P < 0.05$, $^{**}P < 0.01$, $^{***}P < 0.001$, $^{****}P < 0.0001$.

Dynamical system models of neural data

As previously described in published work,[21] we modeled neural activity using recurrent switching linear dynamical systems (rSLDS). Briefly, rSLDS is a generative model that breaks down non-linear time series data into sequences of linear dynamical modes. The model relates three sets of variables: a set of discrete states (z), a set of continuous latent factors (x) that captures the low-dimensional nature of neural activity, and the activity of recorded neurons (y) during male directed behavior (sniffing, dominant mounting and attack). For how the model is formulated, see Nair et al.[21] Model accuracy is evaluated using a forward simulation metric as described in Nair et al.[21] Briefly: given the observed neural activity at time t, we predict the trajectory of the population activity vector over an ensuing short time interval Δt using the model, then compute the mean squared error (MSE) between that trajectory and the observed data at time $t+\Delta t$. This MSE is calculated across all dimensions of the latent space and repeated for all times t. This error metric is normalized to a 0-1 range in each animal across the whole recording and is computed across cross-validation folds to obtain a bounded measure of model performance.

Code used to fit rSLDS on neural data is available in the SSM package: (https://github.com/lindermanlab/ssm)

Code to generate flow fields and energy landscapes from fit dynamical systems is available at (https://github.com/DJALab/VMHvl_MPOA_dynamics)

Visualization of attractor dynamics as 3D landscape

Conversion of the flow-fields obtained from rSLDS into a 3D landscape for visualization by calculating the dynamic velocity at each point in neural state space and using it as the height of a 3D landscape. Dynamic velocity was calculated as previously reported in Nair et al.[21]

Estimation of time constants & calculation of line attractor score

We estimated the time constant of each mode of linear dynamical systems using eigenvalues λ_a of the dynamics matrix of that system as: $\tau_a = \left|\frac{1}{\log(|\lambda_a|)}\right|$ as derived by Maheswaranathan et al.[108] We used a line attractor score computed as $\log_2 \frac{t_n}{t_{n-1}}$ where t_n is the largest time constant of the dynamics matrix of a dynamical system and t_{n-1} is the second largest time constant. In the case of point attractors, the line attractor score is zero due to the similar magnitudes of the first two largest time constants, and it is greater than one for systems that possess a line attractor.

CellPress
OPEN ACCESS

Supplemental figures

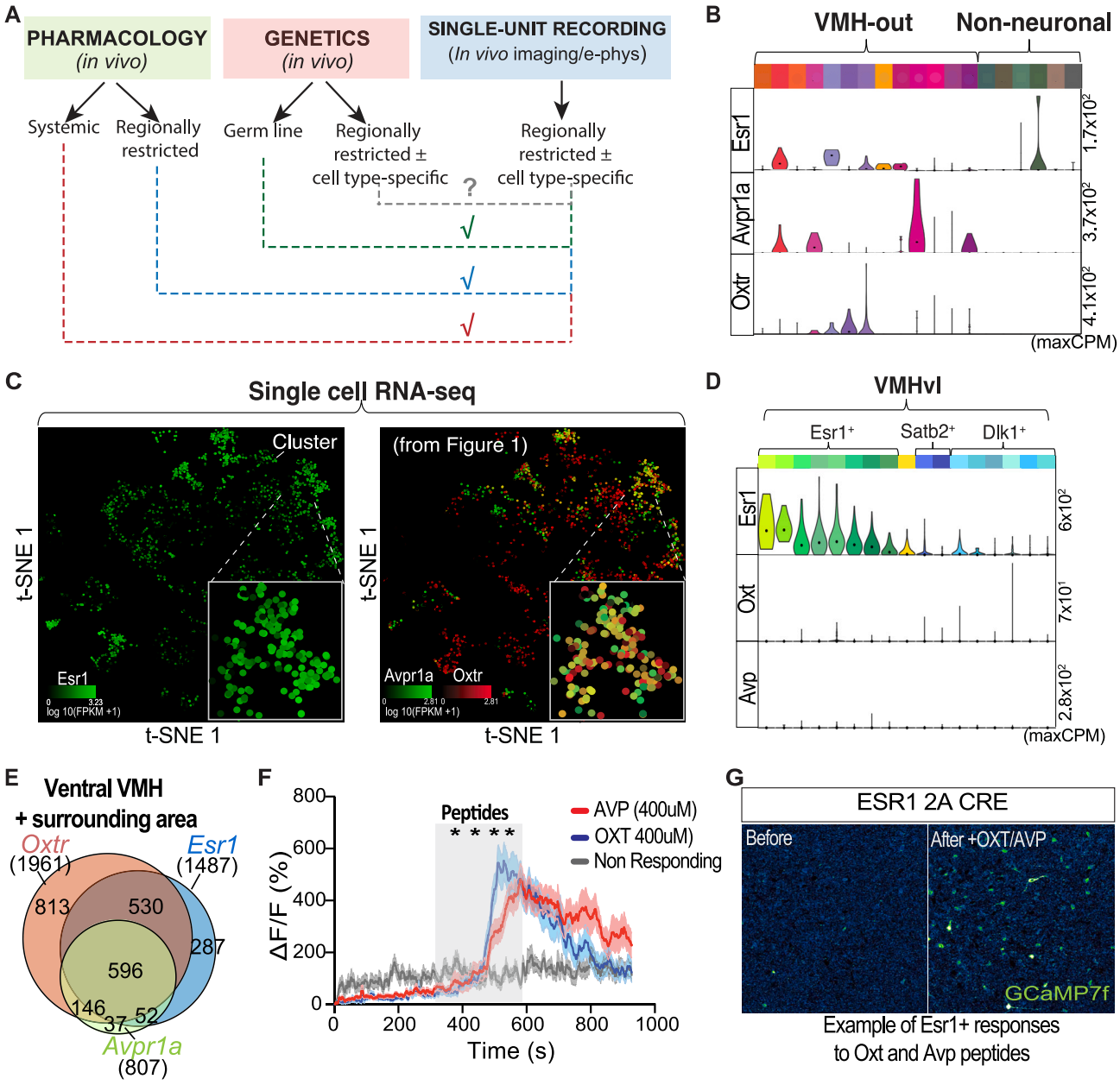

Figure S1. Expression and *ex vivo* functional characterization of *Oxtr* and *Avpr1a* in the VMH, related to Figure 1

(A) A diagram portraying the diverse methodologies employed to investigate neuromodulatory control of neural population activity in mammalian systems. Among the most recent predominant strategies are the systemic administration of agonists/antagonists targeting G-protein-coupled receptors (GPCRs)[109] or the use of knock-out animals combined with electrophysiological recording or calcium imaging approaches.[73] However, there is a need for cell-type-specific, region-restricted, multiplexed gene-editing strategies,[110] compatible with bulk[111–113] or single-cell resolution calcium imaging[114] in freely moving animals.

(B) Violin plots illustrating the expression of *Esr1*, *Avpr1a*, and *Oxtr* mRNAs outside the VMH and in non-neuronal clusters; "max CPM," maximum counts per million reads.

(C) t-SNE plots illustrating the distribution of *Esr1* (i) or *Avpr1a* and *Oxtr* mRNAs (ii) (from Figure 1C) in single cells from the VMH. FPKM, fragments per kilobase of exon per million mapped fragments.

(D) Violin plots illustrating the expression of *Esr1*, *Oxt*, and *Avp* mRNAs in VMHvl; max CPM, maximum counts per million reads.

(legend continued on next page)

(E) Venn diagram of *Esr1, Avpr1a*, and *Oxtr* mRNA-expressing neurons in the ventral part of the VMH and the surrounding areas.
(F) Quantification of Esr1$^+$ responses to 400 nM of Avp (n = 62 cells from 3 mice) or OXT (n = 79 cells from 3 mice). n = 70 cells not activated in brain slices from 3 mice. The shadow area depicts the duration of the bath application of peptides.
(G) An example field of view of spontaneous active (left) and induced Esr1$^+$ GCaMP7f calcium responses to 400 nM OXT and AVP.
Statistics: Kruskal-Wallis test was performed, corrected with Dunn's multiple comparison during time points 300–950 s, and values were plotted as mean ± SEM in (F). ****$p \leq 0.0001$.

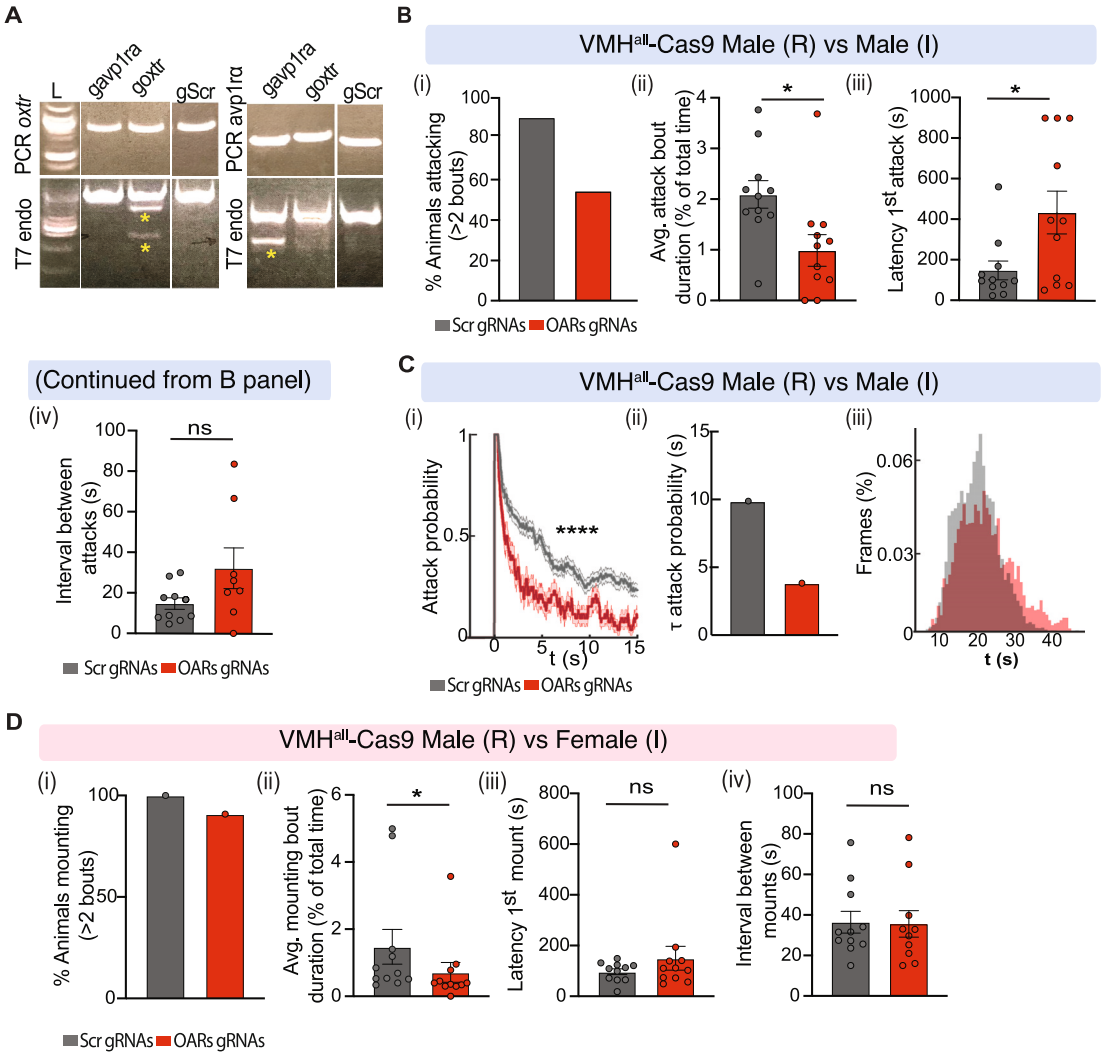

Figure S2. Experimental validation and behavioral characterization of CRISPR-Cas9-based *Oxtr* and *Avpr1a* co-perturbations, related to Figure 2

(A) T7E1-endonuclease treated *Oxtr* (left) and *Avpr1a* (right) PCR products from N2a-Cas9-expressing cells, transfected with gRNAs against *Avpr1a or Oxtr*. As a negative control, a scrambled gRNA (Scr) was used. Yellow stars indicate the cleavage products, indicating successfully induced Cas9-mediated insertions or deletions (INDELs) in the coding sequence complementary to the gRNAs.

(B) Quantification of the percentage of animals attacking (i), the average duration of each attack bout (ii), the latency of the 1st attack bout (iii), and the interval between attack bouts (iv) against a male intruder. n = 11 mice per group.

(C) Quantification of the number and time-varying probability of attack bouts against a male intruder (i and ii). n = 11 mice per group. Quantification of the average velocity during attack in control (n = 9 mice) and experimental mice (n = 8 mice) (iii).

(D) Quantification of the percentage of animals mounting (i), the average duration of each mounting bout (ii), the latency of the 1st mounting bout (iii), and the interval between mounting bouts (iv) in control and experimental mice during male-female interactions. n = 11 mice per group.

Statistics: nested Mann-Whitney test was performed, and values were plotted as mean ± SEM. *$p \leq 0.05$, ****$p \leq 0.0001$.

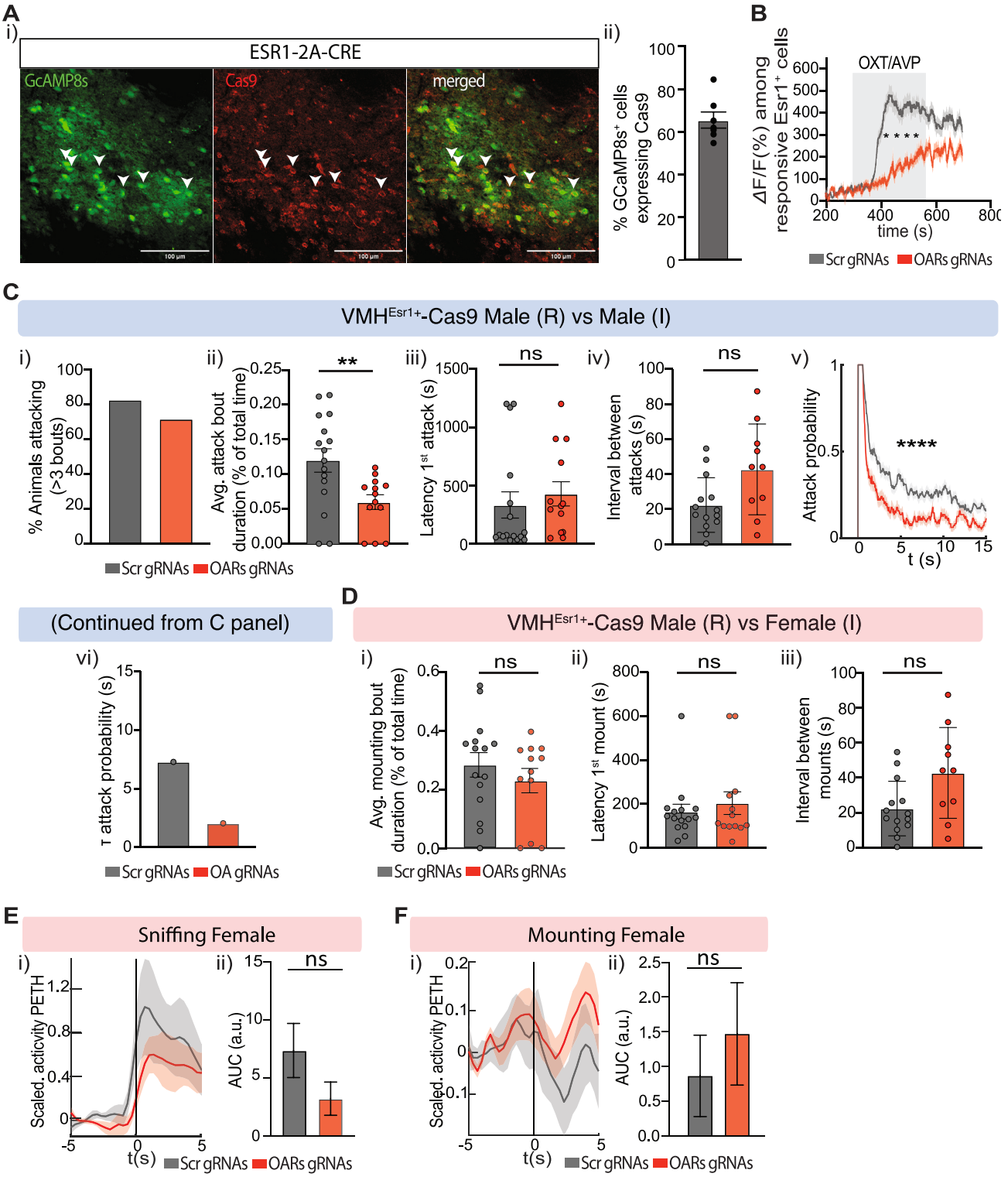

Figure S3. Effects of *Oxtr* and *Avpr1a* co-perturbation on male- and female-directed behaviors and bulk calcium activity, related to Figure 3

(A) Immunostaining against the GCamp8s (green) and Cas9 (red) proteins in coronal hypothalamic sections from ESR1-2A-CRE animals co-injected with a Cre-dependent Cas9 AAV and Cre-dependent gRNA-Gcamp8s AAV. Sections counterstained with DAPI (blue). Arrows depict the expression of Cas9 protein in GCamp8s Esr1 double-positive cells (i). Quantification of GCamp8s-positive cells expressing the Cas9 protein (ii) in the injection site. *n* = 3 mice.

(legend continued on next page)

(B) Quantification of the average activity (ΔF/F) of Esr1^{+} neurons responding to 400 nM of AVP and OXT in brain slices from ESR1-2A-CRE mice co-injected with the Cas9 AAV and Cre-dependent OARs-GCaMP8s AAV (experimental group) or Cre-dependent Scr-GCaMP8s AAV (control group) in the VMHvl (see Figure 3Ai). n = 150 cells from Scr RNA (control) and n = 35 cells from OARs (targeted) slices.
(C) Quantification of the percentage of animals attacking (i), the average duration of each attack bout (ii), the latency of the first attack (iii), the interval between attack bouts (iv), and the number and the time-varying probability (iv and v) of attack bouts during male-male interactions. n = 16 control and n = 13 experimental mice.
(D) Quantification of the average duration of each mounting bout (i), the latency of the first mount (ii), and the interval between mounting bouts (iii) during male-female interactions. n = 15 control and n = 13 experimental mice.
(E) Z scored BTA of VMHvl^{Esr1} activity (i) and the area under the curve (ii) during female-directed sniffing (1 min). n = 4 control and n = 5 experimental mice.
(F) Z scored BTA of VMHvl^{Esr1} activity (i) and the area under the curve (ii) during mounting. n = 3 control and n = 4 experimental mice.
Statistics: Mann-Whitney test was performed, and values were plotted as mean ± SEM. $^{**}p \leq 0.01$, $^{****}p \leq 0.0001$.

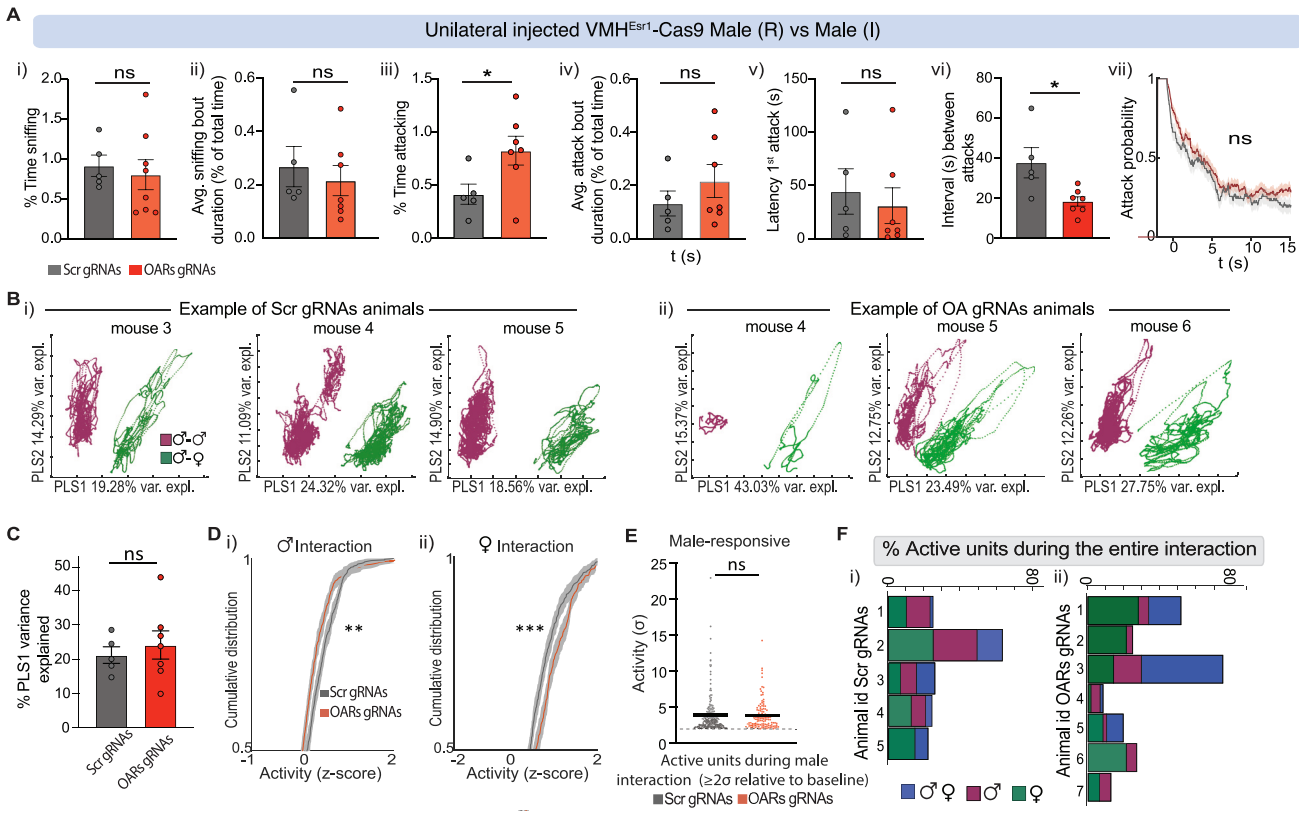

Figure S4. Effect of Oxtr/Avpr1a co-editing on intruder sex-specific representations, single-unit neural activity, and tuning, related to Figure 4

(A) Quantification of the total time spent sniffing (i), the average duration of each sniffing bout (ii), the total time spent attacking (iii), the average duration of each attack bout (iv), the latency of the first attack (v), interval (s) between attack bouts (vi), and the attack probability (vii). n = 5 control and n = 7 experimental unilaterally injected mice.

(B) VMHvl^{Esr1} ensemble representations of intruder sex for control (i) and experimental (ii) mice, projected onto the first two axes of a PLS regression against intruder sex. Traces are colored by intruder sex identity. The percentage of variance explained by the first two PLS components is noted for each male resident.

(C) Quantification of the PLS1 variance explained (which accounts for intruder sex) in control and experimental mice.

(D) Cumulative distribution of Z scored activity of all VMHvl^{Esr1} units during 1 min interaction with male (i) or female (ii) intruders in control and experimental mice.

(E) Average single-unit activity (σ) of male responses (≥ 2σ relative to the pre-intruder baseline) between control and experimental mice.

(F) Percentage of male- or female-selective or co-active units (≥ 2σ relative to the pre-intruder baseline), per imaged control (i) or experimental (ii) mouse. n = 5 control, n = 7 experimental animals.

Statistics: values in (D) are plotted as mean ± SEM. Nested Mann-Whitney test was performed in (C) and (E), while nested Kolmogorov-Smirnov test was used in (D). $^{**}p \leq 0.01$, $^{***}p \leq 0.001$.

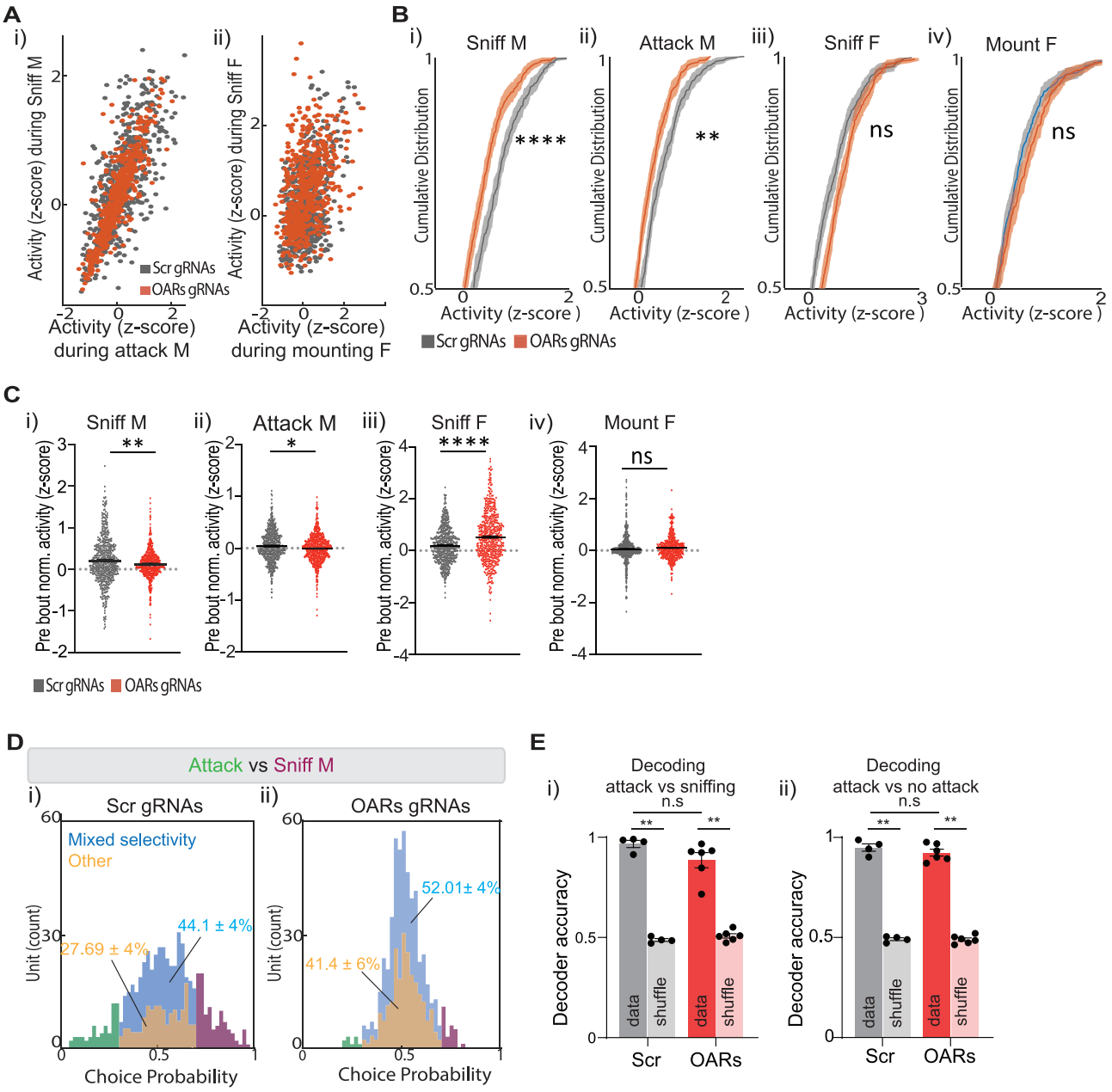

Figure S5. Effect of Oxtr/Avpr1a co-editing on behavior-specific single-unit activity and tuning, related to Figure 5

(A) Scatter plot of the average single VMHvl^{Esr1} unit activity (*Z* score) during male (i) and female (ii) directed behaviors in control and experimental mice.

(B) Cumulative distribution of VMHvl^{Esr1} activity (*Z* score) during male-directed (sniffing and attack; i and ii) and female-directed behaviors (sniffing and mounting; iii and iv) in control and experimental mice.

(C) Average *Z* scored VMHvl^{Esr1} activity normalized to the pre-behavior bout period during male-directed sniffing (i), attack (ii), female-directed sniffing (iii), and mounting (iv).

(D) Choice probabilities histograms of male-directed behaviors (attack vs. sniffing) in control and experimental mice. Mixed-tuned units (blue) and units tuned for other behaviors or not active (yellow) are highlighted.

(E) Accuracy of frame-wise decoders predicting attack vs. sniffing (i) and attack vs. no attack (ii) trained on VMHvl^{Esr1}neural activity in control or experimental animals. Decoders were trained and tested on held-out data from each group separately. $n = 5$ control and $n = 7$ experimental mice.

Statistics: values plotted as mean ± SEM in (B). Nested Kolmogorov-Smirnov test was used in (B), whereas nested Mann-Whitney test was performed in (C) and (E). $^{*}p \leq 0.05$, $^{**}p \leq 0.01$, $^{****}p \leq 0.0001$.

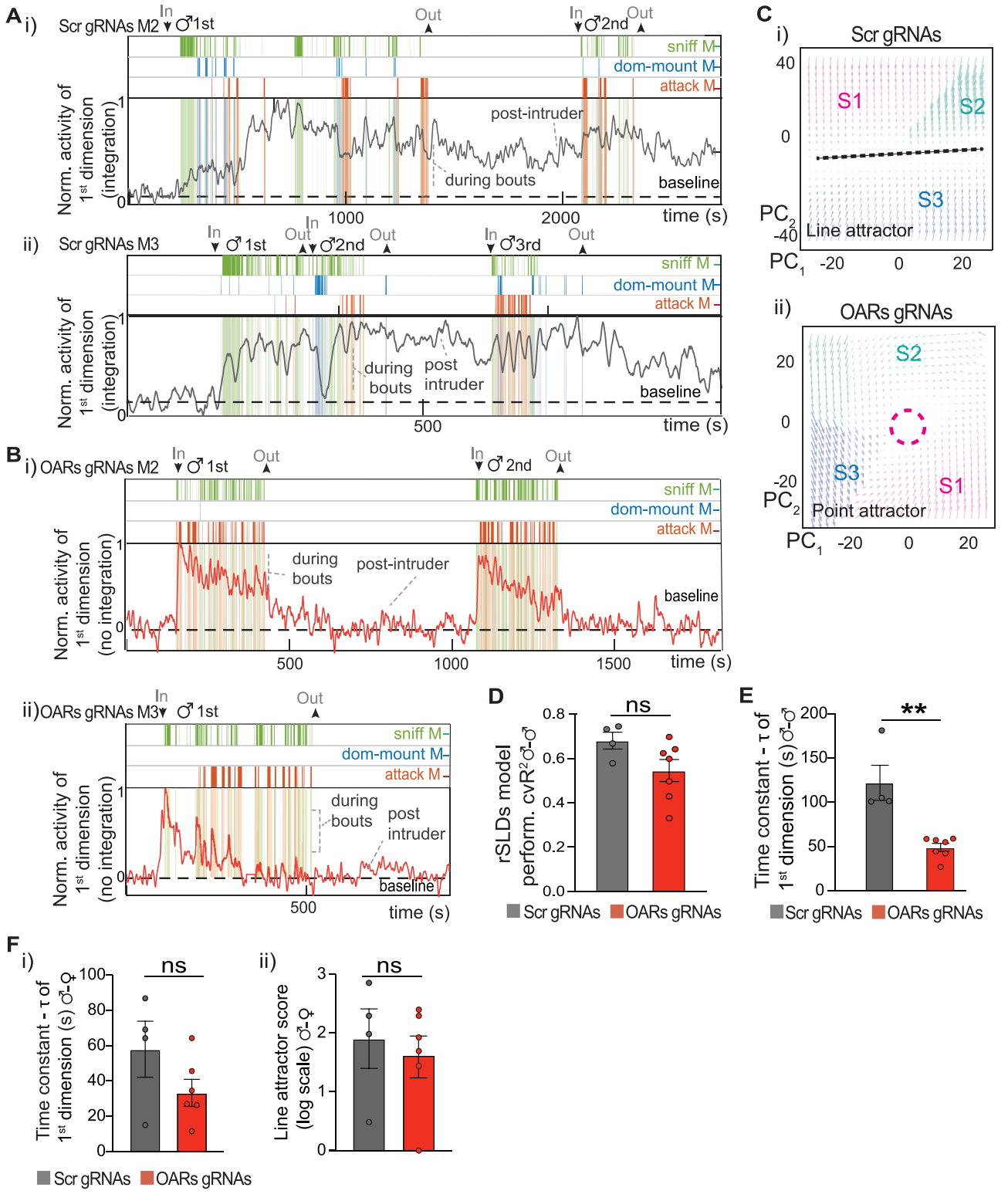

Figure S6. VMHvl^{Esr1} line attractor dynamics require Oxtr/Avpr1a-mediated signaling, related to Figure 6

(A and B) Normalized activity projection onto the time axis of the longest time constant (integration dimension) for VMHvl^{Esr1} units in control (A) and in experimental mice (B).

(legend continued on next page)

(C) Schematic illustrating inferred dynamics shown as flow fields, with the line attractor illustrated by a black dashed line in control (i) and the point attractor with a purple dashed circle in experimental mouse (ii). The different rSLDS states (S1–S3) are depicted with different colors.
(D) Quantification of the performance score for the rSLDS model for each mouse in the control and experimental group during male-male interactions.
(E) Quantification of the average time constant (τ) of the 1st dimension in control and experimental mice during male-male interactions. n = 4 control and n = 7 mutant.
(F) Quantification of the average time constant (τ) of the 1st dimension (i) and the line attractor score (ii) for VMHvl^{Esr} population activity in control and experimental mice during male-female interactions. n = 4 control and n = 6 mutant. All sniffing, dominant mounting, and attack bouts following the introduction of an intruder male are depicted in the behavioral raster plots in (A) and (B).
Statistics: Mann-Whitney test was performed in (D), (E), and (F). $^{**}p \leq 0.01$.

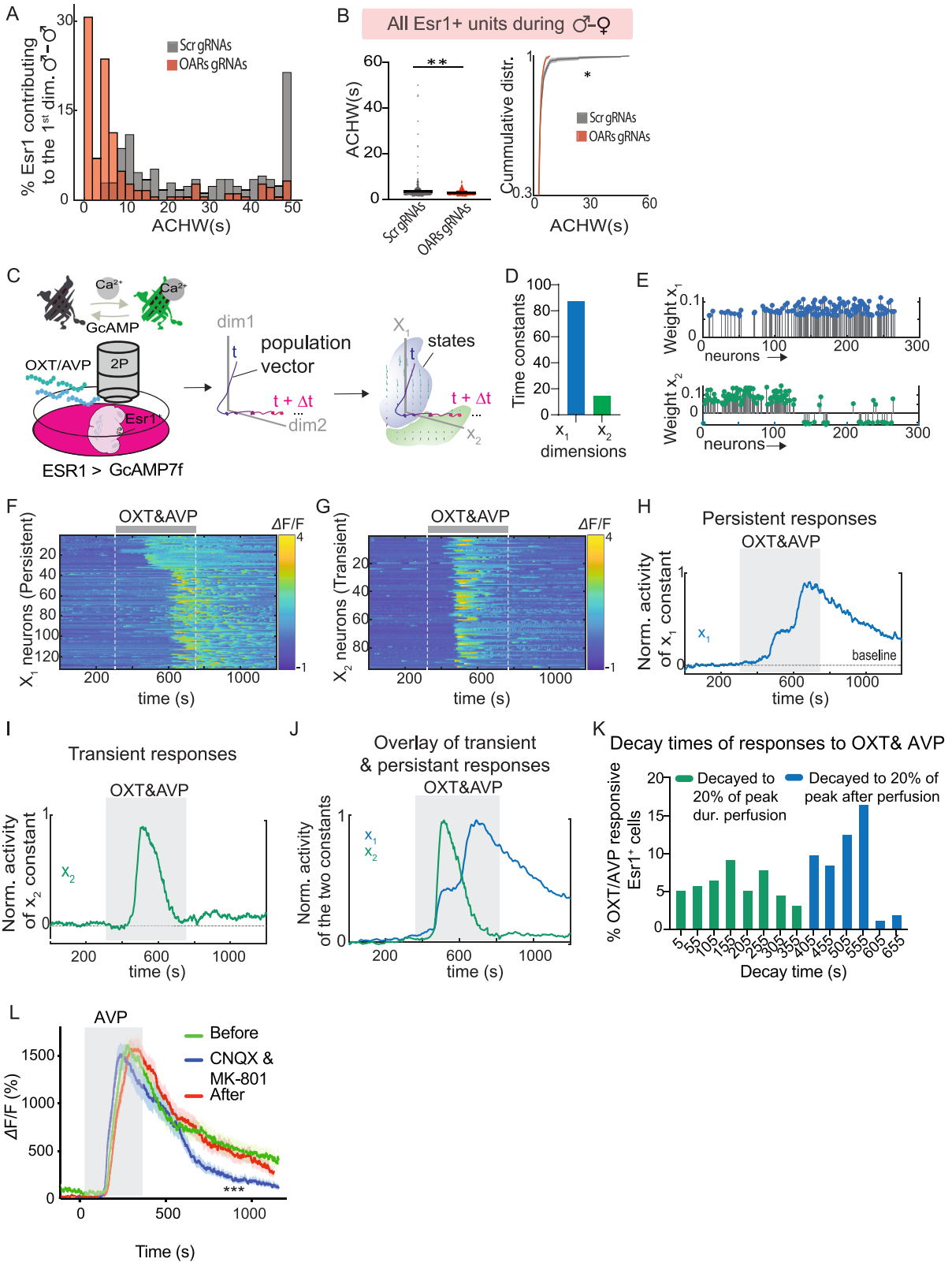

(legend on next page)

Figure S7. OXT and AVP evoke persistent responses in VMHvl^{Esr1} neurons *ex vivo*, related to Figure 7

(A) Distribution plot illustrating the ACHW of VMHvl^{Esr1} units contributing to the 1st dimension during the entire duration of male-male interactions. $n = 4$ control, $n = 7$ experimental animals.

(B) Average single-unit and cumulative distribution of ACHW from all VMHvl^{Esr1} recorded units in control and experimental mice during the first 1–2 min of male-female interactions. $n = 5$ control, $n = 7$ experimental animals.

(C) rSLDS modeling of Esr1^{+} cells calcium responses to 400 nM OXT & AVP. Acute brain slices from male ESR1-2A-CRE animals that express Cre-dependent GCaMP7f were used.

(D) Average time constant of the identified two dimensions (X_1, X_2), arranged in decreasing order for acute brain slices.

(E) Absolute rSLDS weight of neurons contributing to X_1 (top, blue) and X_2 (bottom, green) dimensions sorted by choice probability values for activity during the OXT and AVP perfusion window.

(F and G) Heatmaps of OXT and AVP induced (F) slow persistent X_1 (left) and (G) transient X_2 responses (right) VMHvl^{Esr1} neurons.

(H and I) Projection of population activity onto the time axis of (H) the slow persistent X_1 and (I) the transient X_2 dimensions.

(J) Overlay projection of population activity onto the time axis of the slow persistent X_1 and the transient X_2 dimensions.

(K) Distribution plot illustrating the decay times of Esr1 calcium responses to a 400 nM OXT and AVP cocktail. Cells whose responses decayed to 20% of the peak within the peptide perfusion window were categorized as transient (green), while those responses that decayed to 20% of the peak after the perfusion window were labeled as persistent (blue).

(L) AVP (100 nM)-mediated calcium average responses of VMH slices in the presence of synaptic transmission blockers (20 μM CNQX and 10 μM MK-801; $n = 45$ cells).

Statistics: Kruskal-Wallis test was performed, corrected with Dunn's multiple comparison during time points 0–1,000 s. $^{*}p \leq 0.05$, $^{**}p \leq 0.01$, $^{***}p \leq 0.001$.